

**AD-A283 014**



**Technical Report 1654**  
May 1994

# **Time-Domain Model for a Hydroacoustic Transducer Array**

George W. Benthien  
Don Barach



*scd* **94-24924**

**94 8 05 1 0 1**



Approved for public release; distribution is unlimited.

DTIC QUALITY INSPECTED

**Technical Report 1654**  
May 1994

# **Time-Domain Model for a Hydroacoustic Transducer Array**

George W. Benthien  
Don Barach

**NAVAL COMMAND, CONTROL AND  
OCEAN SURVEILLANCE CENTER  
RDT&E DIVISION  
San Diego, California 92152-5001**

---

**K. E. EVANS, CAPT, USN  
Commanding Officer**

**R. T. SHEARER  
Executive Director**

**ADMINISTRATIVE INFORMATION**

The work was accomplished during the period 1 July 1993 to 31 March 1994 under the sponsorship of the Space and Naval Warfare Systems Command (SPAWAR PMW 182-32).

Released by  
E. F. Rynne, Jr., Head  
Acoustic Analysis Branch

Under authority of  
J. M. Holzmann, Head  
Acoustic Systems and  
Technology Division

**ACKNOWLEDGMENT**

The authors gratefully acknowledge Bob DeLaCroix of Hydroacoustics, Inc., for several helpful discussions concerning their modeling of the HLF-6A transducer and for allowing us access to their computer code which we used to compare with our results. We also gratefully acknowledge some helpful suggestions by Dr. Steven Black of the Naval Research Laboratory/Underwater Sound Reference Detachment.

# EXECUTIVE SUMMARY

## OBJECTIVES

To develop a mathematical model for a transducer array which can handle nonlinear devices such as the HLF-6A hydraulic transducers. The model should be capable of handling both sinusoidal and nonsinusoidal electrical inputs.

## APPROACH

Since the model must be able to handle nonlinear devices it is necessary to formulate the model in the time domain rather than in the frequency domain. The internal components of the transducers were modeled using standard hydraulic flow equations which are in the form of nonlinear ordinary differential equations. The equations are nonlinear since the pressure drop across a hydraulic valve is proportional to the square of the flow through the valve. The acoustic radiation interaction impedances were obtained in the frequency domain using the boundary element program CHIEF. The frequency-domain interaction impedances were then transformed to the time domain using an FFT routine to produce interaction impulse responses. The radiation impedance relations in the frequency domain become convolution relations in the time domain. When these radiation convolution integral relations are combined with the model for the transducer internal components, the result is a coupled set of nonlinear differential-integral equations that is solved numerically by an explicit time-stepping procedure similar to a second-order Runge-Kutta method.

## RESULTS

Our time-domain model was first applied to an array of simple linear transducers for which the solution could be obtained by conventional frequency-domain methods. The agreement between the results of our time-domain model and the frequency-domain results was excellent. A comparison was also made between our model and a model developed by Hydroacoustics, Inc. for a single transducer element. Again the agreement was quite good. Finally, predicted results using our time-domain model were compared with experimental results for a three-element close-packed array. The agreement was reasonably good in both level and trends.

# CONTENTS

<b>EXECUTIVE SUMMARY</b>	iii
<b>1 INTRODUCTION</b>	1
<b>2 LINEAR MODEL</b>	2
2.1 BASIC EQUATIONS . . . . .	2
2.2 SOLUTION PROCEDURE . . . . .	7
2.3 RESULTS . . . . .	8
<b>3 HYDROACOUSTIC MODEL</b>	16
3.1 FIRST-STAGE SERVOVALVE . . . . .	16
3.2 SECOND-STAGE VALVE . . . . .	20
3.3 PRESSURE COMPENSATION . . . . .	24
3.4 RADIATING DISKS AND DRIVE CAVITY . . . . .	26
3.5 SUMMARY OF EQUATIONS . . . . .	28
3.6 RESULTS . . . . .	29
<b>4 CONCLUSIONS AND RECOMMENDATIONS</b>	44
<b>5 REFERENCES</b>	45

<b>Accession For</b>	
NTIS GR&I	<input checked="" type="checkbox"/>
DTIC TAB	<input type="checkbox"/>
Unannounced	<input type="checkbox"/>
Justification	
By	
Distribution/	
Availability Codes	
Avail and/or	
Special	
Dist	
A-1	1

## LIST OF FIGURES

1	Simple linear transducer element. . . . .	2
2	Mutual velocity impulse coefficient for a pair of elements ( $d/s = 2$ ). . . . .	4
3	Self-acceleration impulse response ( $d/s = 2$ ). . . . .	5
4	Mutual acceleration impulse response $\mu_{12}$ ( $d/s = 2$ ). . . . .	5
5	Mutual acceleration impulse response $\mu_{13}$ ( $d/s = 2$ ). . . . .	6
6	Three-element array configuration. . . . .	9
7	Velocity magnitude of outer element of three-element array. . . . .	11
8	Velocity phase of outer element of three-element array. . . . .	11
9	Velocity magnitude of middle element of three-element array . . . . .	12
10	Velocity phase of middle element of three-element array. . . . .	12
11	Time response of a single element in the free field ( $s/\lambda = 0.110$ ). . . . .	13
12	Middle element of three-element array, $Q=\infty$ . . . . .	13
13	Middle element of three-element array, $Q=100$ . . . . .	14
14	Middle element of three-element array, $Q=20$ . . . . .	14
15	Middle element of three-element array, $Q=10$ . . . . .	15
16	Idealized hydroacoustic transducer. . . . .	17
17	First-stage servovalve and associated drive circuit. . . . .	18
18	Second-stage valve. . . . .	21
19	Supply port geometry. . . . .	22
20	Single element, $-6$ dB drive level. . . . .	32

21	Single element, -3 dB drive level. . . . .	32
22	Single element, 0 dB drive level. . . . .	33
23	Single element, 3 dB drive level. . . . .	33
24	Single element, -6 dB drive level, HAI load model. . . . .	34
25	Single element, -3 dB drive level, HAI load model. . . . .	34
26	Single element, 0 dB drive level, HAI load model. . . . .	35
27	Single element, 3 dB drive level, HAI load model. . . . .	35
28	NRaD impedance magnitude comparison. . . . .	36
29	NRaD impedance phase comparison. . . . .	36
30	HAI impedance magnitude comparison. . . . .	37
31	HAI impedance phase comparison. . . . .	37
32	Impedance magnitude, NRaD vs HAI, frequency-domain model. . . . .	38
33	Impedance phase, NRaD vs HAI, frequency-domain model. . . . .	38
34	Impedance magnitude, NRaD vs HAI, time-domain model. . . . .	39
35	Impedance phase, NRaD vs HAI, time-domain model. . . . .	39
36	Source level for three-element array, experiment vs computed. . . . .	40
37	Normalized source level, single element vs array. . . . .	40
38	Velocity of middle element of three-element array at freq=FL. . . . .	41
39	Drive cavity pressure of middle element of three-element array at freq=FL. . . . .	41
40	Velocity comparison, middle element of 1 × 6 array vs single element. . . . .	42
41	Drive cavity pressure comparison, middle element of 1 × 6 array vs single element. . . . .	42

42 Normalized source level, single element vs six-element array. . . . . 43

## LIST OF TABLES

1 Normalized variables. . . . . 9

# 1 INTRODUCTION

This report contains a description of a mathematical model for a hydroacoustic transducer array. Although the model was developed with the HLF-6A transducer in mind, it can be applied to other hydroacoustic transducer arrays. This model is based partly on previous modelling work for the HLF-4 transducer [1], but involves new work relating to acoustic radiation loading. Previous models have attempted to couple frequency-domain models for the acoustic field with time-domain models for the internal components of the transducer. In this report we present a complete time-domain model for the coupled transducer/acoustic-field problem which is applicable to both single elements and arrays. This model can also handle nonsinusoidal signals, which is important since linear superposition is not valid for nonlinear devices. The acoustic radiation model involves obtaining certain interaction coefficients in the frequency domain with a boundary element program called CHIEF [2,3] and then transforming these coefficients to the time domain by using Fourier transforms. When these coefficients are combined with a model for the internal components, the result is a coupled set of differential-integral equations that can be solved by an explicit time-stepping procedure with prescribed initial conditions.

Since the model for acoustic radiation loading is new, it was first applied to a simple linear transducer array for which the solution could also be obtained by the standard frequency-domain approach. Section 2 contains a description of the linear model that includes the new acoustic radiation approach. Results of the time-domain model are compared with corresponding frequency-domain results in order to validate the new acoustic radiation approach. The agreement was excellent. Section 3 contains a description of the models for the various components of the HLF-6A hydraulic transducer, such as the first-stage servovalve, the second-stage valve, the drive cavity, the radiating disks, the pressure compensation device, and the radiation loading. Although the equations for this transducer are more complicated than those for the simple linear transducer, the form of the equations and the general solution procedure are essentially the same. Computed results for a single HLF-6A transducer in water are compared with computed results for the Hydroacoustics, Inc. (HAI) model when several drive levels are used and when the input signal is sinusoidal in time. The agreement is quite good for all drive levels, but there are some small departures at the higher drive levels (less than 1 dB), which we attribute to differences in the radiation models. Results are also presented for a proposed six-element array. Since the interelement spacing for this array is quite large, the performance of each element is not greatly different from that of a single element in the free field. Predicted results using our time-domain model are also compared with experimental results for a three-element array which is fairly closely packed. The comparison is reasonably good both in level and in trends. Section 4 is a summary of our conclusions and recommendations.

## 2 LINEAR MODEL

In this section a time-domain radiation model will be developed and applied to a simple linear transducer. The resulting linear model will be used to validate the time-domain approach to the acoustic radiation loading which will later be applied to the nonlinear HLF-6A hydroacoustic transducer. The simple linear transducer is shown in figure 1. It consists of two rigid circular pistons of mass  $M$  placed symmetrically at the ends of a rigid cylindrical housing. A spring of stiffness  $K$  restrains each piston and each piston is driven by the same prescribed force  $F$ .

Subsection 2.1 gives the mass/spring relations for this simple linear transducer as well as a time-domain formulation for acoustic loading on the transducer. The result is a system of coupled differential-integral equations with specified initial conditions. The solution procedure for solving this system is described in subsection 2.2. In subsection 2.3 the results for a three-element array are compared with those from a frequency-domain model after the initial transients have died out, in order to validate the time-domain formulation.

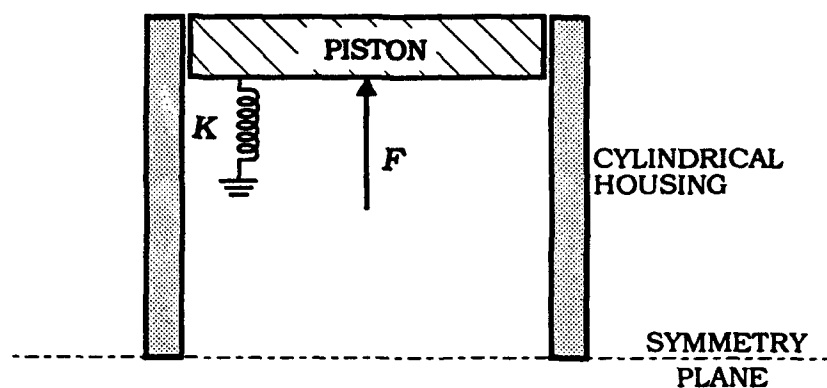


Figure 1. Simple linear transducer element.

### 2.1 BASIC EQUATIONS

The differential equation describing this simple device is

$$M\ddot{u} + Ku = F - F^{rad} \quad (1)$$

where  $F^{rad}$  is the acoustic radiation force on the piston and  $u$  is the displacement of the piston. The acoustic radiation force is given by

$$F^{rad} = \int_A p dA \quad (2)$$

where  $p$  is the acoustic pressure and  $A$  is the surface of the piston in contact with the water. Now consider a planar array of  $N$  of these elements. The radiation force on the  $m$ -th element of an array can be expressed as a linear function of the piston normal velocities. In the frequency domain this relation takes the form

$$F_m^{rad}(\omega) = \sum_{n=1}^N z_{mn}(\omega) v_n(\omega) \quad (3)$$

where  $F_m^{rad}$  is the radiation force on the  $m$ -th element,  $z_{mn}$  is the mutual radiation impedance between the  $m$ -th and  $n$ -th elements, and  $v_n$  is the velocity of the  $n$ -th piston. These acoustic interaction impedances  $z_{mn}$  are obtained by using the boundary element program CHIEF, which is based on the Helmholtz integral equation

$$\frac{1}{2}p(\zeta) = \int_S [p(\sigma) \frac{\partial G}{\partial n}(\zeta, \sigma) + i\omega\rho v(\sigma)G(\zeta, \sigma)] dS \quad (4)$$

where  $S$  is the radiating surface (including all array elements),  $v$  is the normal velocity,  $\rho$  is the fluid density, and  $G$  is the free-space Green's function. To obtain  $z_{mn}$  the integral equation 4 is solved for  $p$  when all the piston velocities are set to zero except for  $v_n$ , which is set to 1. The resulting pressure is integrated over the  $m$ -th piston, yielding  $z_{mn}$ .

When the interaction relation in equation 3 is transformed into the time domain via a Fourier transform, it takes the form

$$F_m^{rad}(t) = r_m^\infty v_m(t) + \sum_{n=1}^N \int_0^t \zeta_{mn}(\tau) v_n(t - \tau) d\tau \quad (5)$$

where  $\zeta_{mn}$  is the Fourier transform of  $z_{mn}$  for  $m \neq n$ ,  $r_m^\infty$  is the real, high-frequency asymptotic limit of  $z_{mm}$ , and  $\zeta_{mm}$  is the Fourier transform of  $z_{mm} - r_m^\infty$ . It turns out that for numerical reasons it is better to work with accelerations than with velocities. The conversion of the interaction equations 3 and 5 from velocities to accelerations gives the frequency-domain relation

$$F_m^{rad}(\omega) = \sum_{n=1}^N m_{mn}(\omega) a_n(\omega) \quad (6)$$

and the time-domain relation

$$F_m^{rad}(t) = \sum_{n=1}^N \int_0^t \mu_{mn}(\tau) a_n(t - \tau) d\tau \quad (7)$$

where  $m_{mn}(\omega) = z_{mn}(\omega)/i\omega$  and

$$\mu_{mn}(t) = \int_0^t \zeta_{mn}(\tau) d\tau \quad m \neq n \quad (8)$$

$$= \int_0^t \zeta_{mm}(\tau) d\tau + r_m^\infty \quad m = n \quad (9)$$

Figure 2 is a plot of the impulse interaction coefficient  $\zeta_{12}$  appearing in equation 5 versus normalized time. This plot illustrates the reason for expressing the convolution integrals in terms of acceleration instead of velocity. The fact that the functions  $\zeta_{mn}$  ( $m \neq n$ ) alternate in sign over a very short interval gives rise to subtraction errors when the convolution integrals are evaluated. Figures 3-5 show the mutual impulse functions  $\mu_{11}$ ,  $\mu_{12}$ , and  $\mu_{13}$  appearing in equation 7 versus normalized time. Notice that these functions are significantly nonzero only over a small time interval (nominally the time for sound to travel across both the interacting elements). To obtain the mutual impulse functions  $\mu_{mn}$ , the CHIEF [3] program was used to calculate the mutual radiation impedances  $z_{mn}$  over a broad frequency range. The mutual impedances were divided by  $i\omega$  and transformed to the time domain by using an FFT routine. The self-impulse function  $\mu_{mm}$  has a discontinuity at  $t = 0$ . To eliminate the resulting high-frequency oscillation in the computed  $\mu_{mm}$ , we use the fact that the even extension of a time function has a Fourier transform which is twice the real part of the original transform. Thus,  $\mu_{mm}$  can be computed by taking the FFT of twice the real part of  $z_{mm}/i\omega$ .

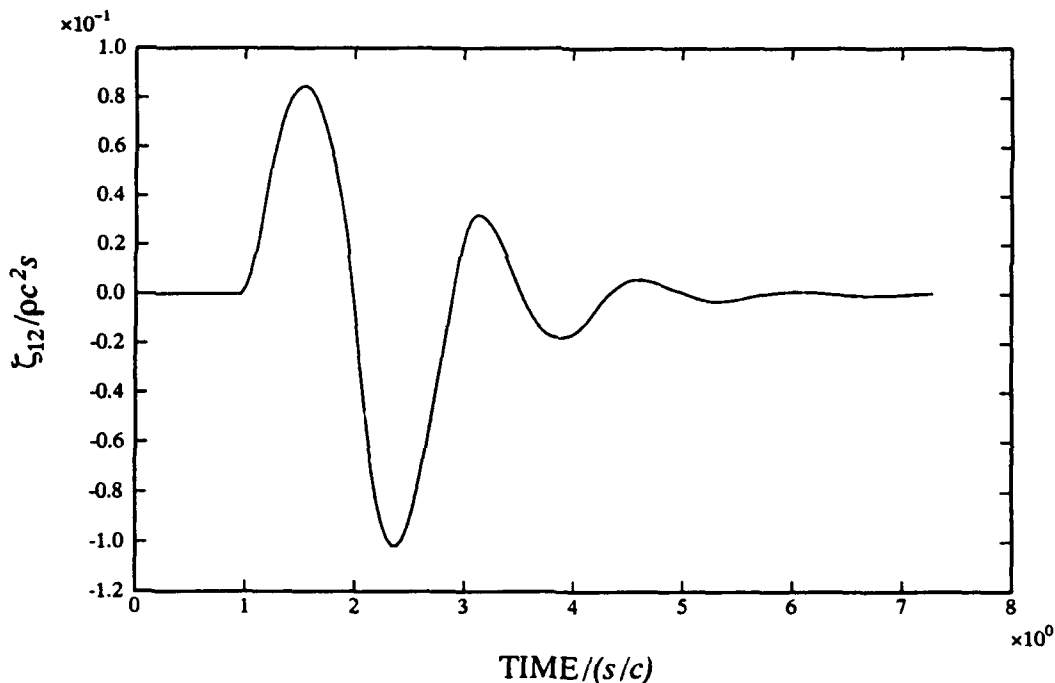


Figure 2. Mutual velocity impulse coefficient for a pair of elements ( $d/s = 2$ ).

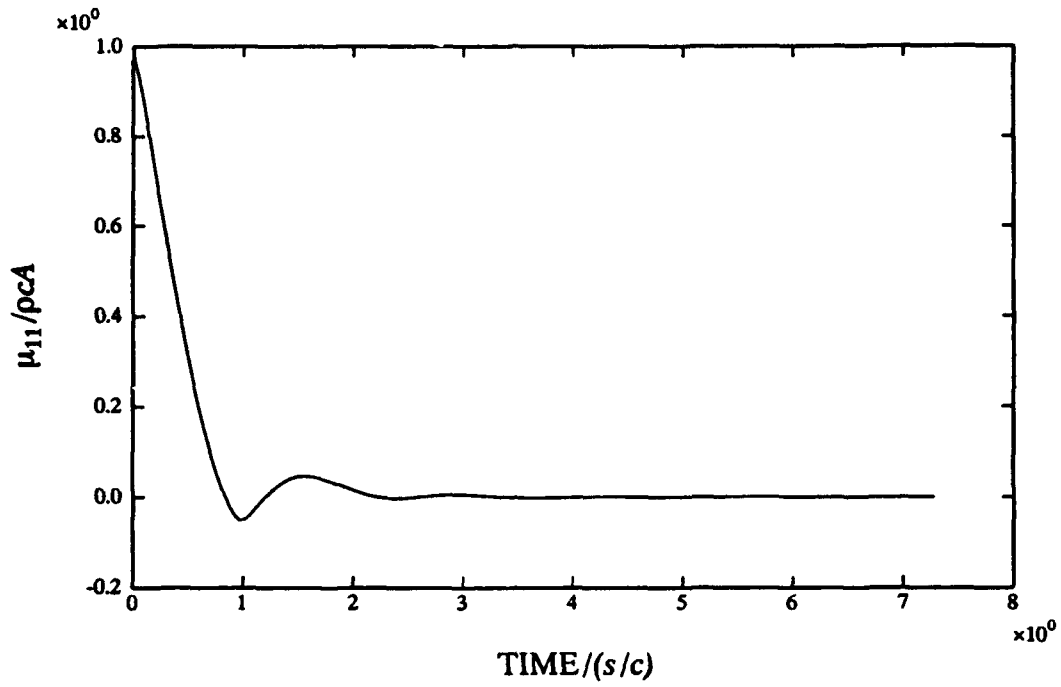


Figure 3. Self-acceleration impulse response ( $d/s = 2$ ).

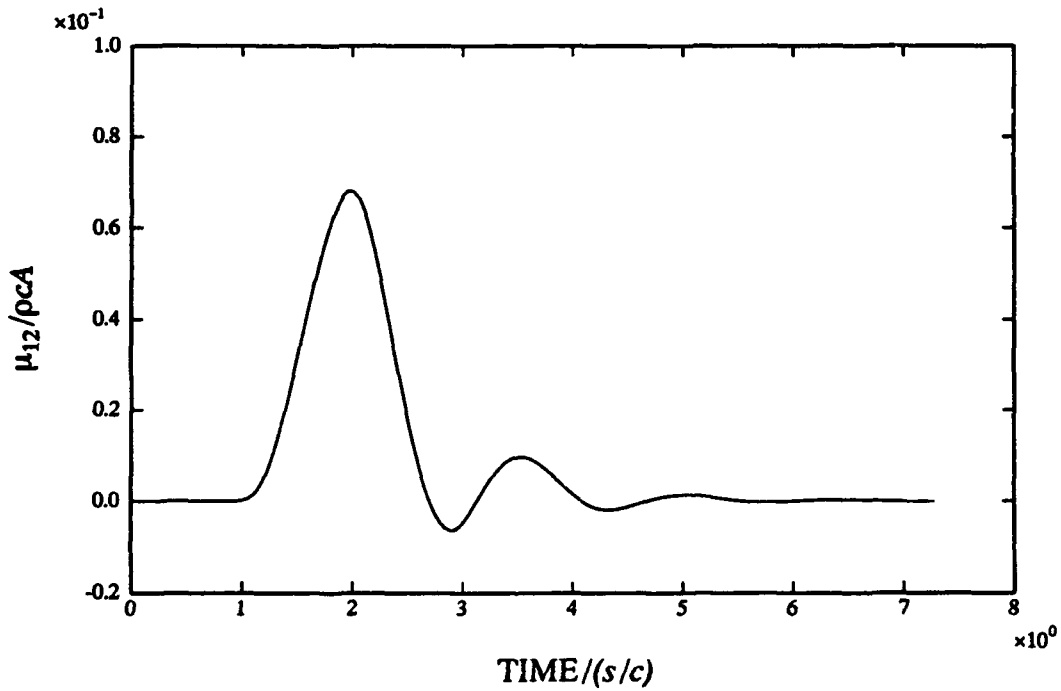


Figure 4. Mutual acceleration impulse response  $\mu_{12}$  ( $d/s = 2$ ).

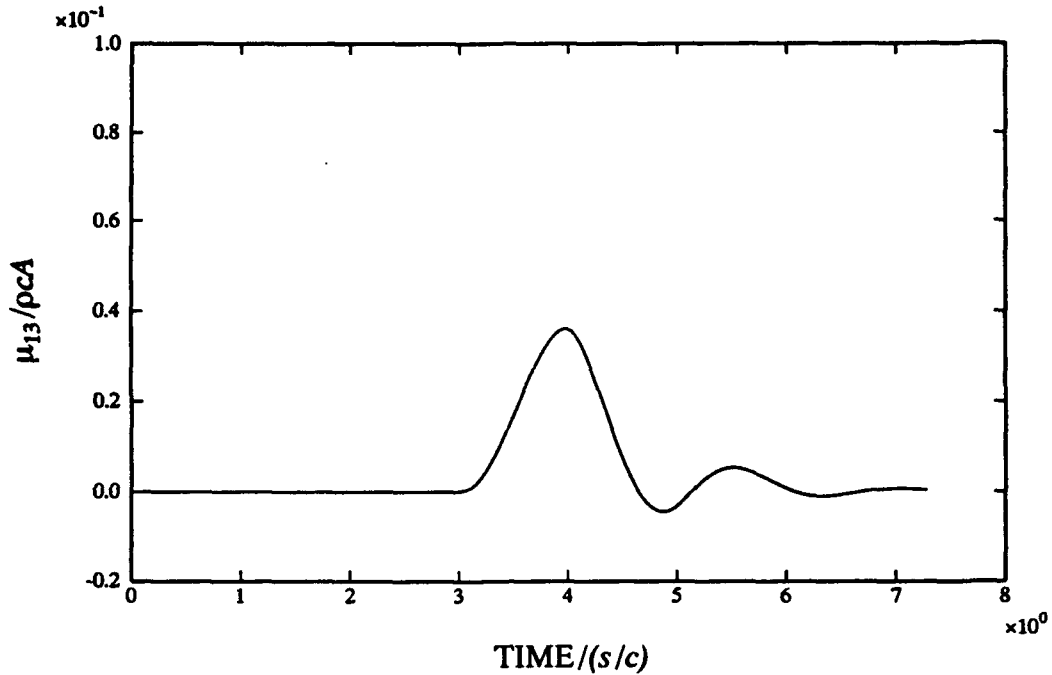


Figure 5. Mutual acceleration impulse response  $\mu_{13}$  ( $d/s = 2$ ).

Combining the acoustic interaction equation 7 with the element equation 1 gives the following coupled system of differential and integral equations:

$$M a_m + K u_m = F_m - \sum_{n=1}^N \int_0^t \mu_{mn}(\tau) a_n(t - \tau) d\tau \quad (10a)$$

$$\dot{v}_m = a_m \quad (10b)$$

$$\dot{u}_m = v_m \quad m = 1, \dots, N \quad (10c)$$

where  $F_m$  is the prescribed force on the  $m$ -th element. Notice that there is a set of equations like 10 for each element in the array and that these sets of equations are coupled through the convolution integrals in 10a that involve histories of all the element accelerations. It will be assumed that the elements are not moving before  $t = 0$  and thus

$$u_m(0) = v_m(0) = a_m(0) = 0 \quad m = 1, \dots, N \quad (11)$$

The differential-integral equations 10 and the initial conditions 11 describe the problem to be solved numerically.

## 2.2 SOLUTION PROCEDURE

In this section a solution procedure will be described for the coupled set of integral-differential equations 10. As with systems of ordinary differential equations, the solution is advanced successively by time steps of length  $\delta$  beginning at the initial time  $t = 0$ . To describe the method it is only necessary to specify how the solution is advanced from a time  $t_r = r\delta$  to the next time  $t_{r+1} = t_r + \delta$ .

It will be convenient to first write the equation 10a in a somewhat different form. When  $t$  is in the interval  $[t_r, t_{r+1}]$  the integrals in 10a can be split as follows:

$$\int_0^t \mu_{mn}(\tau) a_n(t - \tau) d\tau = \int_0^{t-t_r} \mu_{mn}(\tau) a_n(t - \tau) d\tau + \int_{t-t_r}^t \mu_{mn}(\tau) a_n(t - \tau) d\tau \quad (12)$$

An element in the array does not feel the effects of its neighboring elements immediately since there is a time delay required for sound to travel between the elements. Thus,  $\mu_{mn}(t) = 0$  for  $t \leq d_{min}/c$ , where  $d_{min}$  is the minimum distance between any two elements and  $c$  is the sound speed. It will be assumed in what follows that the time step  $\delta$  is smaller than  $d_{min}/c$ . With this assumption

$$\int_0^{t-t_r} \mu_{mn}(\tau) a_n(t - \tau) d\tau = 0 \quad m \neq n \quad (13)$$

since  $t - t_r \leq \delta \leq d/c$ . When  $m = n$  the first integral in equation 12 can be approximated using the trapezoidal rule as follows:

$$\int_0^{t-t_r} \mu_{mm}(\tau) a_m(t - \tau) d\tau \doteq \frac{1}{2} [\mu_{mm}(0) a_m(t) + \mu_{mm}(t - t_r) a_m(t_r)] (t - t_r) \quad (14)$$

It follows from equations 12 to 14 that

$$\begin{aligned} \sum_{n=1}^N \int_0^t \mu_{mn}(\tau) a_n(t - \tau) d\tau &= \frac{1}{2} [\mu_{mm}(0) a_m(t) + \mu_{mm}(t - t_r) a_m(t_r)] (t - t_r) + \\ &\sum_{n=1}^N \int_{t-t_r}^t \mu_{mn}(\tau) a_n(t - \tau) d\tau \end{aligned} \quad (15)$$

Substituting 15 into equation 10a and solving for  $a_m$  yields

$$a_m(t) = \frac{1}{M + \frac{1}{2} \mu_{mm}(0)(t - t_r)} \left[ F_m(t) - K u_m(t) - \frac{1}{2} \mu_{mm}(t - t_r) a_m(t_r) (t - t_r) - \sum_{n=1}^N \int_{t-t_r}^t \mu_{mn}(\tau) a_n(t - \tau) d\tau \right] \quad (16)$$

Combining 16 with the last two equations of 10, we obtain

$$\dot{u}_m(t) = \frac{1}{M + \frac{1}{2}\mu_{mm}(0)(t - t_r)} \left[ F_m(t) - K u_m(t) - \frac{1}{2}\mu_{mm}(t - t_r)a_m(t_r)(t - t_r) - \sum_{n=1}^N \int_{t-t_r}^t \mu_{mn}(\tau)a_n(t - \tau) d\tau \right] \quad (17a)$$

$$\dot{u}_m(t) = v_m(t) \quad (17b)$$

Notice that the right-hand side of equation 17 involves only the two unknown functions  $u_m$ ,  $v_m$ , and past values of  $a_m$  which are known at this stage.

The systems of equations 17 can be solved in the same manner as a system of ordinary differential equations. The only modification necessary is to update the accelerations  $a_m$  at the end of each step by using equation 16. It should be pointed out that a time step must be completed for each element in the array before the next time step is addressed. It is necessary to store the time histories of the accelerations for each element in the array and to update these histories following each time step. Since the  $\mu_{mn}$ 's are essentially zero outside a small time interval, only the relevant portions of the time histories need to be saved.

The results to be presented later in this paper were obtained using a second-order Runge-Kutta method known as Heun's method [4]. For a system of ordinary differential equations

$$\dot{y}(t) = f(y(t), t) \quad (18a)$$

$$y(0) = y_0 \quad (18b)$$

This solution procedure advances the solution  $y_n$  at time  $t_n$  to the solution  $y_{n+1}$  at time  $t_{n+1}$  by using

$$y_{n+1} = y_n + \frac{1}{2} \left[ \dot{y}_n + f(y_n + \dot{y}_n \delta, t_{n+1}) \right] \delta \quad (19)$$

The algorithm given by equation 19 together with the formulas for updating accelerations can be used to solve the differential-integral equations given in equation 17.

## 2.3 RESULTS

In this section we will present computed results for a single element and for a  $1 \times 3$  array as shown in figure 6.

The results will be checked against those obtained from an independent frequency-domain analysis. With the dimensionless variables defined in table 1, equation 10 can be written as follows:

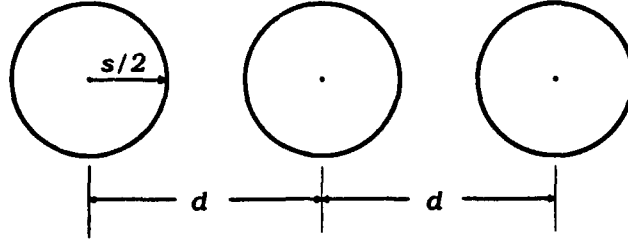


Figure 6. Three-element array configuration.

$$\bar{M}\bar{a}_m + \bar{K}\bar{u}_m = \bar{F}_m - \sum_{n=1}^N \int_0^{\bar{t}} \bar{\mu}_{mn}(\bar{\tau})\bar{a}_n(\bar{t} - \bar{\tau}) d\bar{\tau} \quad (20a)$$

$$\frac{d\bar{v}_m}{d\bar{t}} = \bar{a}_m \quad (20b)$$

$$\frac{d\bar{u}_m}{d\bar{t}} = \bar{v}_m \quad m = 1, \dots, N \quad (20c)$$

Table 1. Normalized variables.

$\bar{t} = \frac{t}{s/c}$	time	$\bar{F}(\bar{t}) = \frac{1}{\rho s^2 c^2} F(st/c)$	drive force
$\bar{u}(\bar{t}) = \frac{1}{s} u(st/c)$	displacement	$\bar{\mu}(\bar{t}) = \frac{1}{\rho c s^2} \mu(st/c)$	$\mu$
$\bar{v}(\bar{t}) = \frac{1}{c} v(st/c)$	velocity	$\bar{M} = \frac{M}{\rho s^3}$	mass
$\bar{a}(\bar{t}) = \frac{s}{c^2} a(st/c)$	acceleration	$\bar{K} = \frac{K}{\rho c^2 s}$	stiffness

The dimensionless parameters in equation 20 were chosen to make the low-frequency radiation mass of the circular piston equal to the mass of the piston and to make the piston diameter one-tenth of a wavelength at the resonance frequency. This leads to the dimensionless parameters

$$\bar{M} = \frac{1}{3} \quad \bar{K} = \frac{2\pi^2}{75} \quad (21)$$

The dimensionless forcing functions  $\bar{F}_m$  were taken to have the form

$$\begin{aligned}\bar{F}_m(\bar{t}) &= \frac{|F_m|}{\rho c^2 s^2} \sin(\omega t) \\ &= \frac{|F_m|}{\rho c^2 s^2} \sin\left(2\pi \frac{s}{\lambda} \bar{t}\right)\end{aligned}\quad (22)$$

where  $\lambda$  is the acoustic wavelength. In the numerical examples the force amplitudes  $|F_m|/\rho c^2 s^2$  were taken to be 1. The spacing  $d$  between elements for the array example was taken to be  $2s$ .

Figures 7-10 show a comparison of the frequency response of the outer and middle elements of the  $1 \times 3$  array when both a frequency-domain approach and a time-domain approach are used. The agreement is very good. Figure 11 shows the solution of the differential-integral equations 10 for a single element. The steady-state normalized velocity amplitude for this computed solution and the value obtained from a steady-state frequency-domain analysis of this problem were both 15.5. Figure 12 shows the computed time response for the middle element in the  $1 \times 3$  array. Due to the large number of oscillations in the given time interval only the envelope of the response is discernible. It takes a very long time for the response to reach steady state (about 300 times as long as it takes sound to travel across the array).

Figures 13-15 show the effect of adding an increasing amount of damping resistance to the linear transducer model. The  $Q$  values given are for the element operating in a vacuum and are thus a measure of the internal resistance. As the internal losses increase, the level of the response decreases and the time to reach steady state decreases. The effect of losses is important since hydroacoustic transducers typically have very high internal losses.

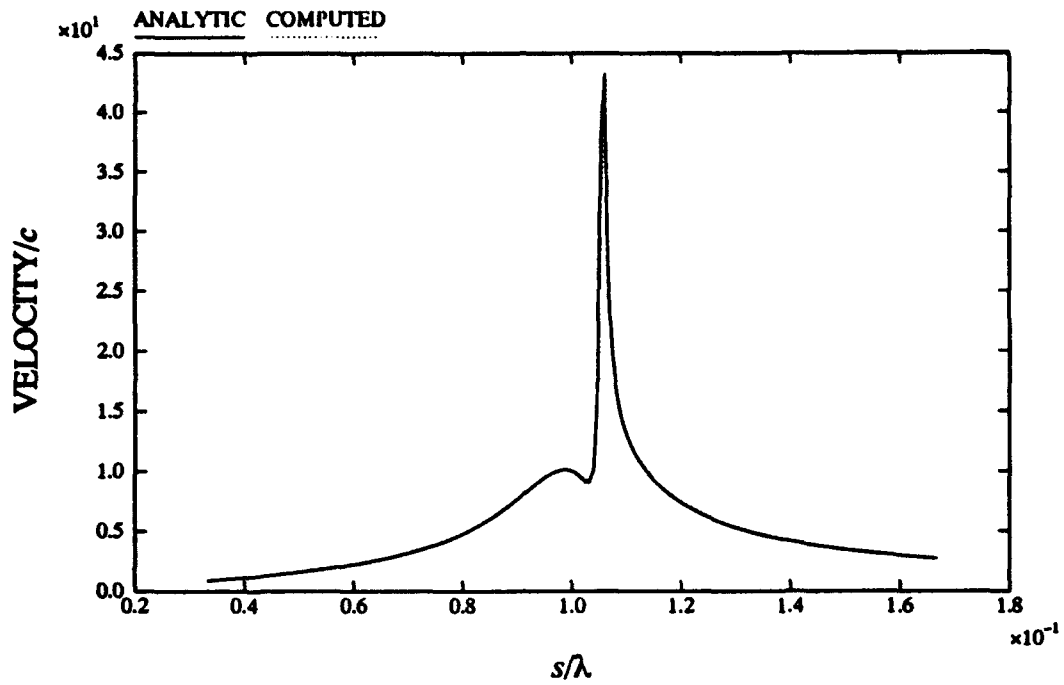


Figure 7. Velocity magnitude of outer element of three-element array.

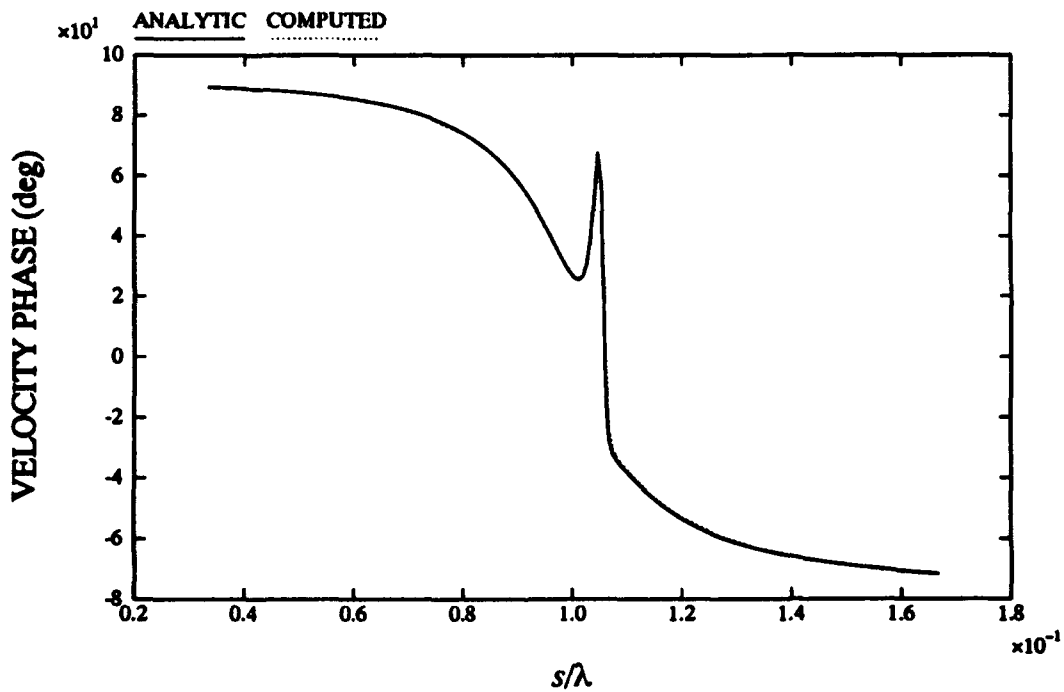


Figure 8. Velocity phase of outer element of three-element array.

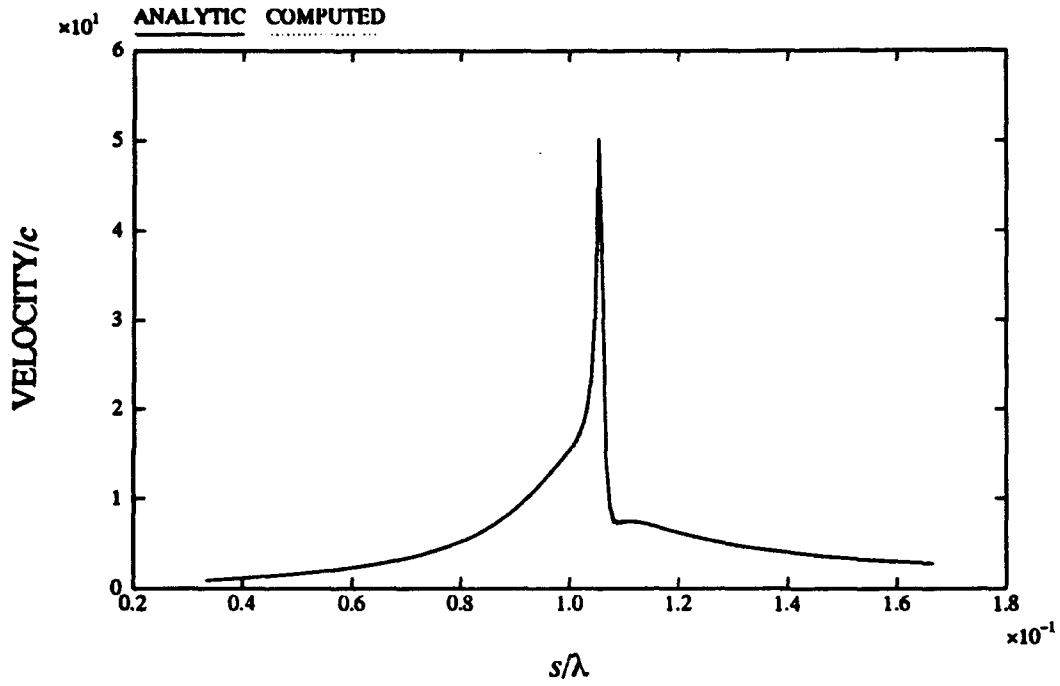


Figure 9. Velocity magnitude of middle element of three-element array

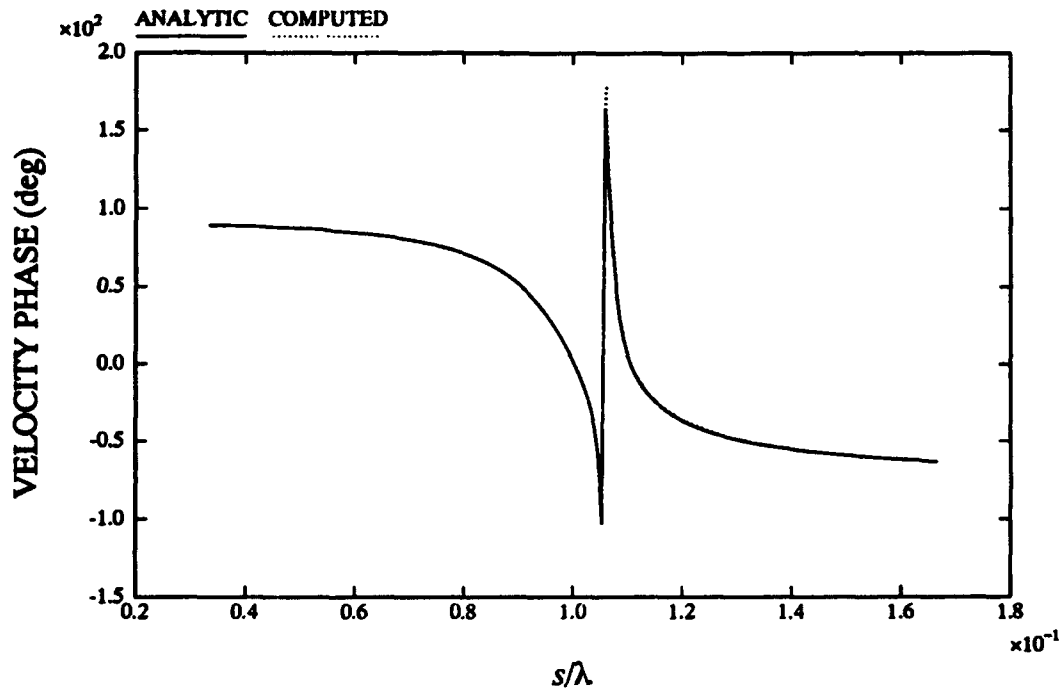


Figure 10. Velocity phase of middle element of three-element array.

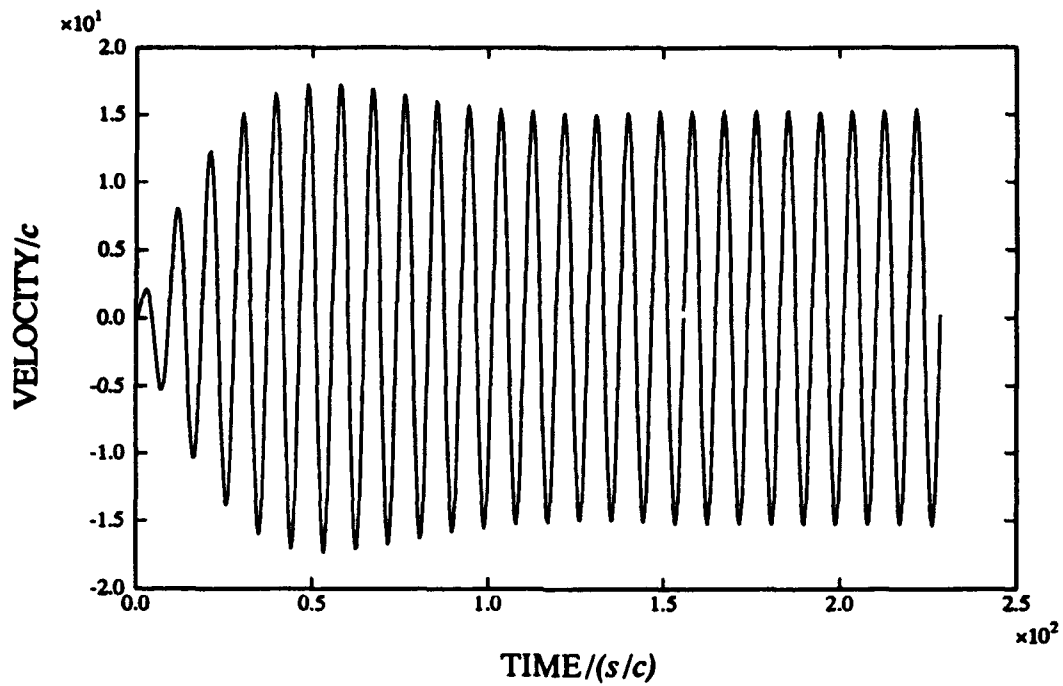


Figure 11. Time response of a single element in the free field ( $s/\lambda = 0.110$ ).

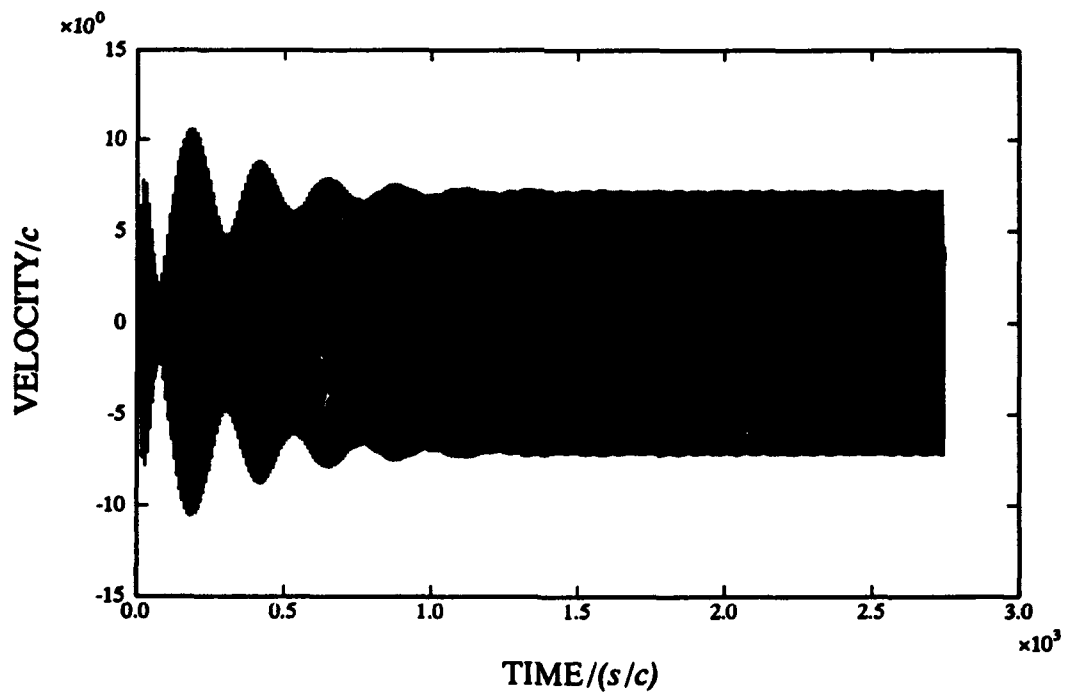


Figure 12. Middle element of three-element array,  $Q=\infty$ .

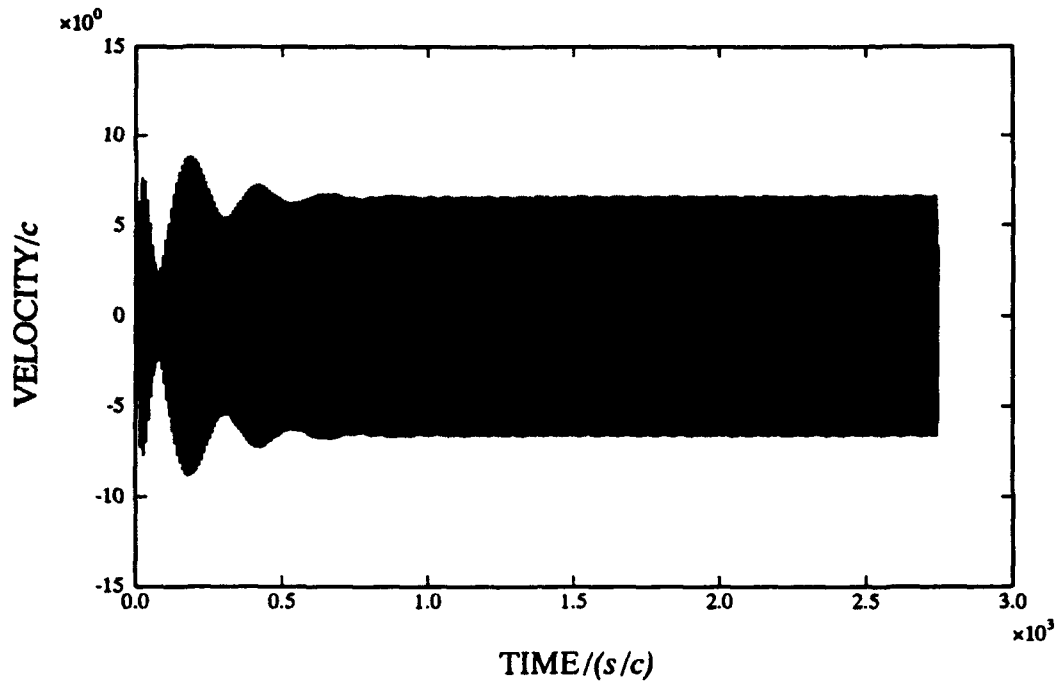


Figure 13. Middle element of three-element array,  $Q=100$ .

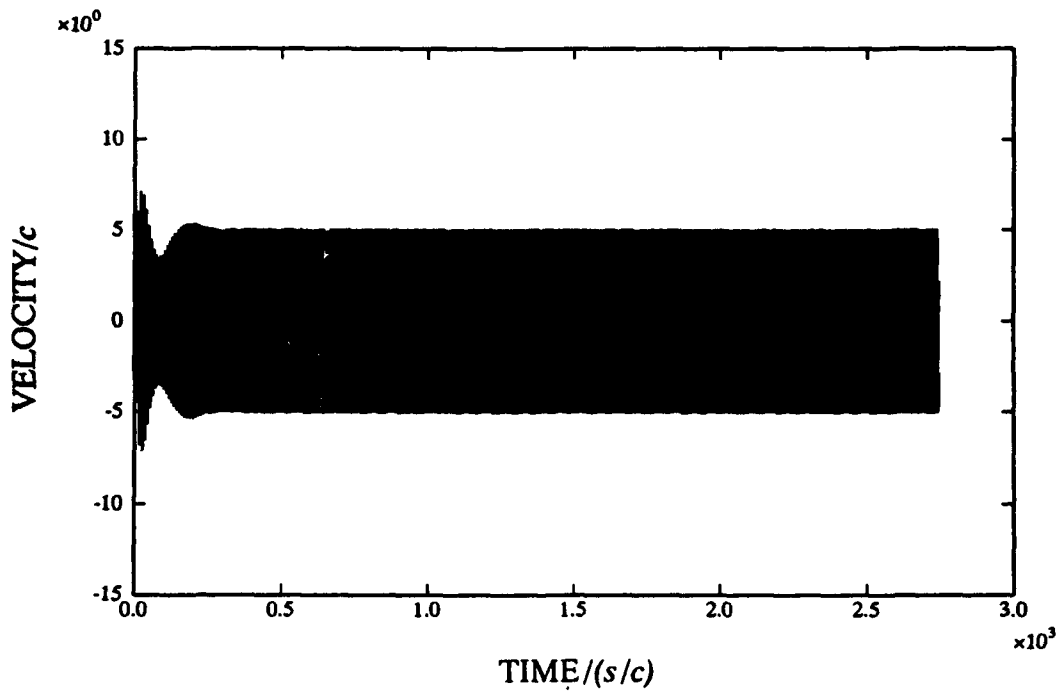


Figure 14. Middle element of three-element array,  $Q=20$ .

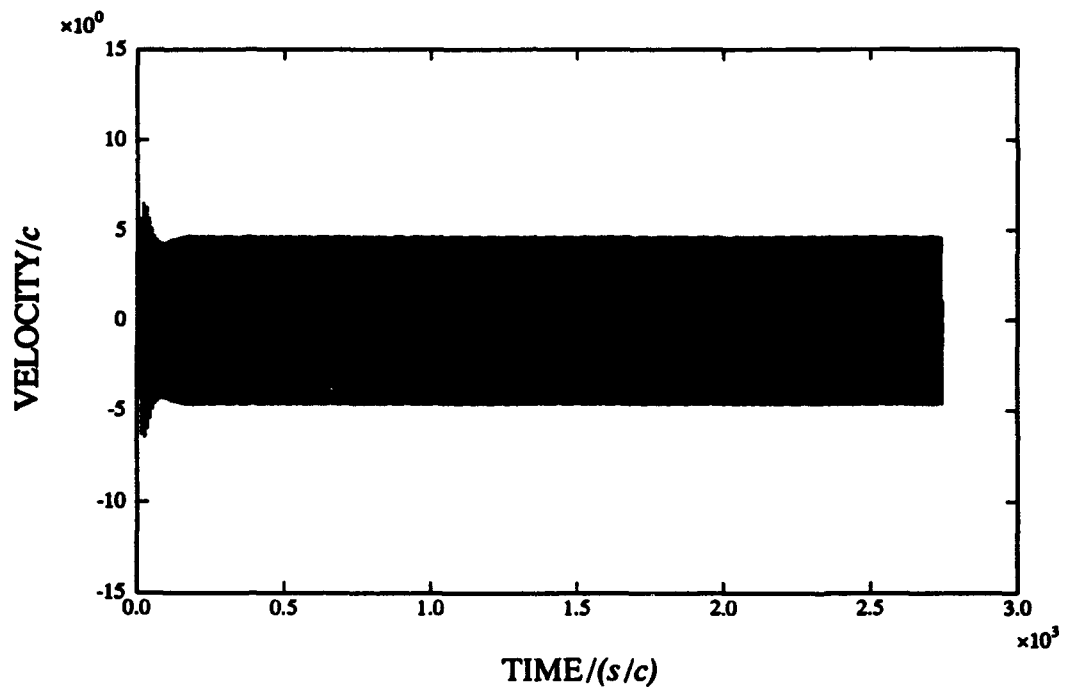


Figure 15. Middle element of three-element array,  $Q=10$ .

### 3 HYDROACOUSTIC MODEL

Figure 16 is an idealized representation of the internal components of a hydroacoustic transducer like the HLF-6A. The transducer consists of two metallic radiating disks which are clamped around their circumference to a cylindrical housing. The disks are driven at their centers by two drive pistons, which in turn are driven by the pressure in an oil-filled drive cavity. The drive cavity pressure is modulated by a sliding valve that controls the flow into and out of the cavity. This valve is driven by a hydraulic servovalve. The servovalve is called the first-stage valve and the main valve is called the second-stage valve. As the second-stage valve slides back and forth, the drive cavity is alternately coupled to the supply and return ports of a hydraulic pump. The pump is designed to maintain a constant pressure at the supply port. The supply pressure is much higher than the return pressure.

This section contains descriptions of the mathematical models for the main components of the HLF-6A transducer. The equations for the first-stage servovalve are given in subsection 3.1 and the equations for the second-stage valve are given in subsection 3.2. The equations for the added stiffness due to the pressure compensation mechanism are given in subsection 3.3. The mathematical model for the radiating disks, drive cavity, and the acoustic loading is presented in subsection 3.4. The model for the acoustic loading is a straightforward extension of the model previously described for the simple linear transducer. A summary of the differential-integral equations for an array of hydroacoustic elements is presented in subsection 3.5. Subsection 3.6 presents results obtained from this model for both single elements and arrays. Single-element results are compared with those of an existing HAI model for various drive levels. Results for a proposed six-element array are compared with those of a single element. Model results for a close-packed three-element array are compared with experimental results.

#### 3.1 FIRST-STAGE SERVOVALVE

This section describes a mathematical model for the first-stage servovalve used in the HLF-6A and its associated drive circuit. A diagram of the servovalve and drive circuit is shown in figure 17.

The internal components of the servovalve (enclosed by a dotted box in figure 17) were not modeled in detail. Instead an empirical relationship of the form

$$x_{sv} = K_{sv}I \quad (23)$$

was used to relate the drive current  $I$  and the servovalve displacement  $x_{sv}$ . We will next show how to relate the servovalve displacement to the servovalve output flow  $Q_v$  and the

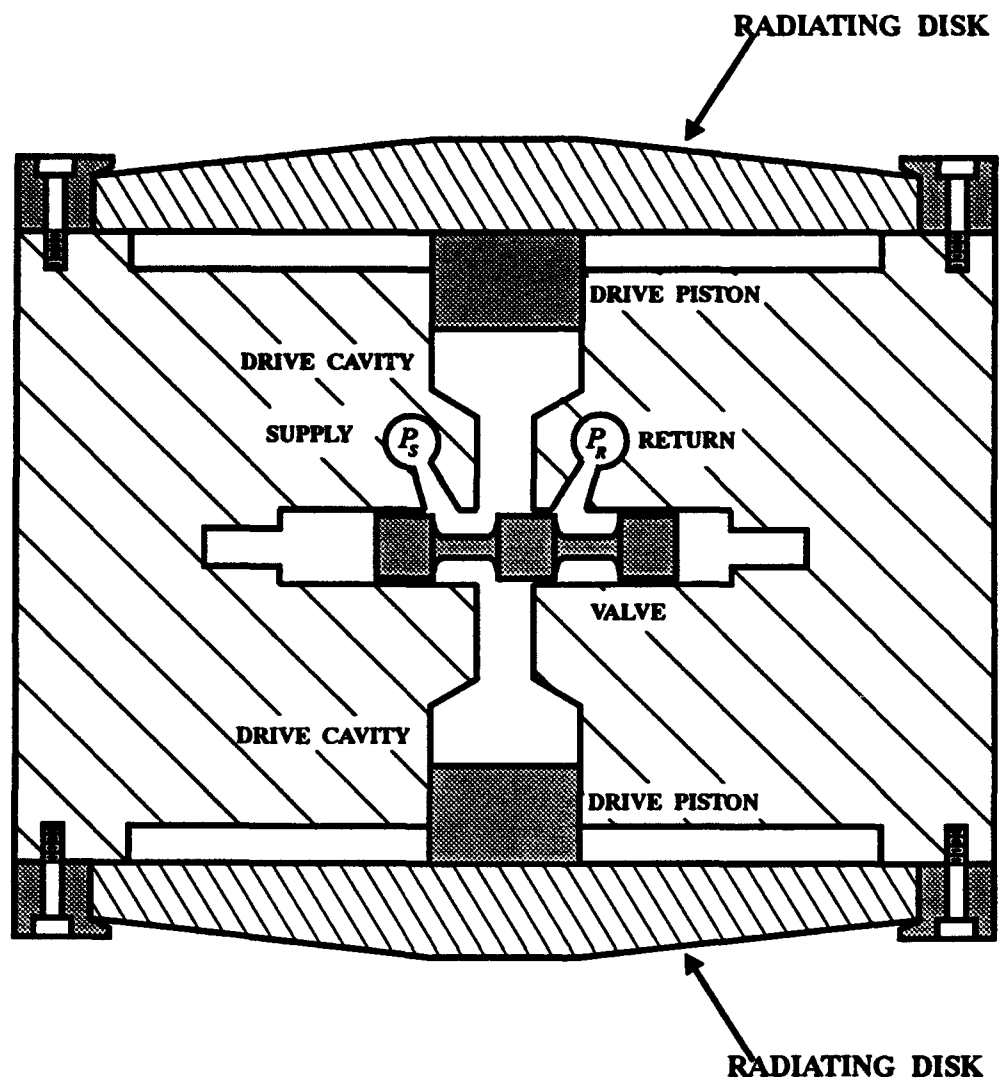


Figure 16. Idealized hydroacoustic transducer.

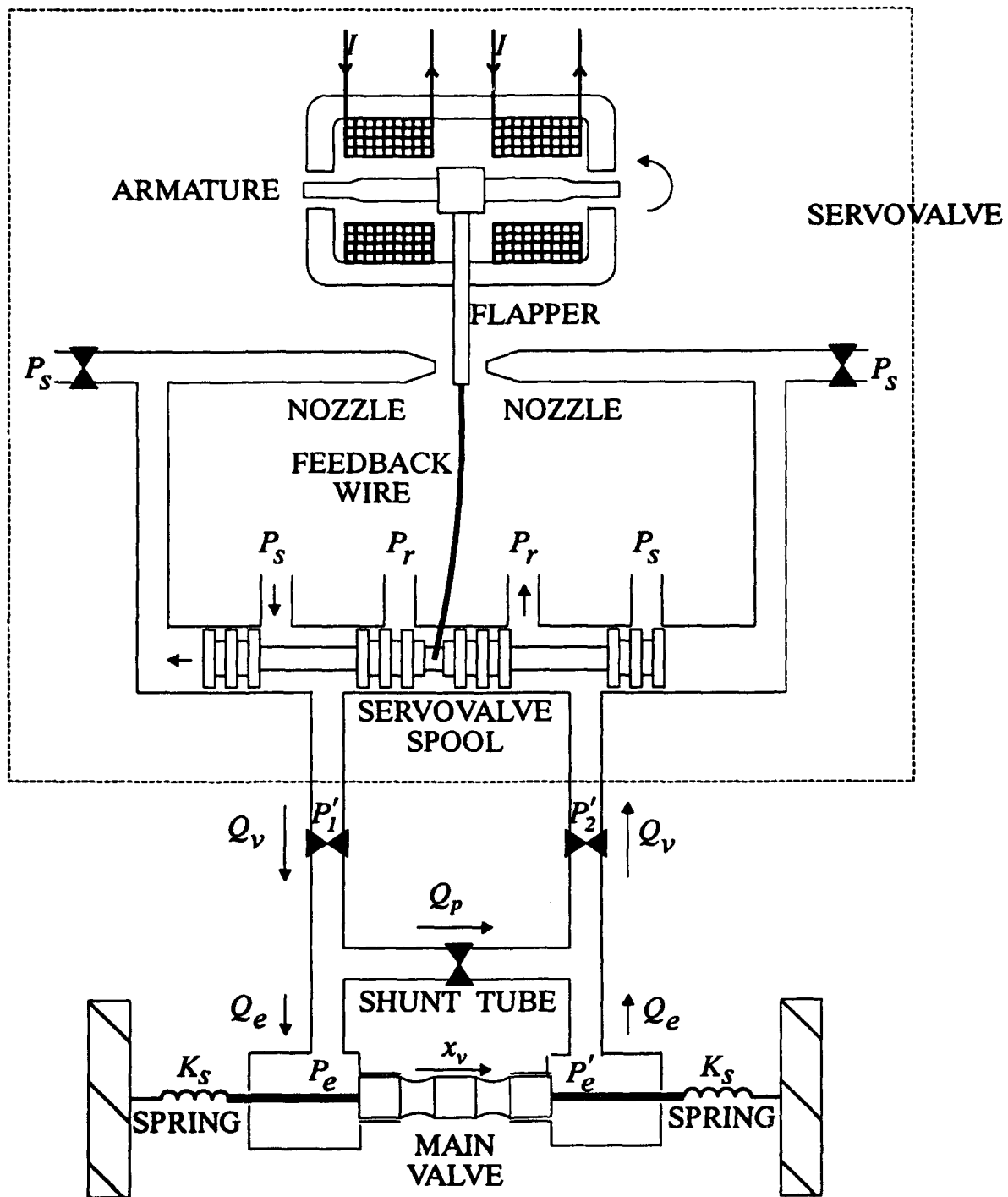


Figure 17. First-stage servovalve and associated drive circuit.

main valve displacement  $x_v$ . Let us define  $P_1$  and  $P_2$  as follows:

$$P_1 = \begin{cases} P_s & \text{if } x_{sv} \geq 0 \\ P_r & \text{if } x_{sv} < 0 \end{cases} \quad P_2 = \begin{cases} P_r & \text{if } x_{sv} \geq 0 \\ P_s & \text{if } x_{sv} < 0 \end{cases} \quad (24)$$

Then the flow  $Q_v$  through the servovalve satisfies the equations

$$P_1 - P'_1 = P'_2 - P_2 = I_v \frac{\beta Q_v^2}{x_{sv}^2} \quad (25)$$

where  $I_v$  is the sign of  $Q_v$  and  $\beta$  is a constant that depends on the geometry of the valve and the density of the fluid. Thus

$$I_v Q_v \geq 0 \quad (26)$$

The flow  $Q_v$  also satisfies the orifice equations

$$P'_1 - P_e = P'_e - P'_2 = I_v \alpha_1 Q_v^2 \quad (27)$$

where  $\alpha_1$  depends on the geometry of the two identical output orifices and on the density of the fluid. The flow  $Q_p$  through the shunt orifice satisfies

$$P_e - P'_e = I_s \alpha_2 Q_p^2 \quad (28)$$

where  $I_s$  is the sign of  $Q_p$  and  $\alpha_2$  is a constant that depends on the geometry of the shunt orifice and on the density of the fluid. The flows  $Q_v$ ,  $Q_e$ , and  $Q_p$  also satisfy the balance equation

$$Q_v = Q_p + Q_e \quad (29)$$

It follows from equation 29 that

$$I_s Q_p = I_s (Q_v - Q_e) \geq 0 \quad (30)$$

Addition of the equations 25, 27, and 28 yields the equation

$$P_1 - P_2 = I_s \alpha_2 Q_p^2 + 2I_v \alpha_1 Q_v^2 + 2I_v \frac{\beta Q_v^2}{x_{sv}^2} \quad (31)$$

Combining equations 29 and 31 gives

$$P_1 - P_2 = I_s \alpha_2 (Q_v - Q_e)^2 + 2I_v \alpha_1 Q_v^2 + 2I_v \frac{\beta Q_v^2}{x_{sv}^2} \quad (32)$$

or

$$\left( I_s \alpha_2 + 2I_v \alpha_1 + 2I_v \frac{\beta}{x_{sv}^2} \right) Q_v^2 - (2I_s \alpha_2 Q_e) Q_v + (I_s \alpha_2 Q_e^2 - P_1 + P_2) = 0 \quad (33)$$

The quadratic equation 33 has the solutions

$$Q_v = \frac{-B + I_v \sqrt{B^2 - 4AC}}{2A} \quad (34)$$

where  $I_r = \pm 1$  and

$$A = I_s + 2I_v \left( \alpha_1 + \frac{\beta}{x_{sv}^2} \right) \quad (35a)$$

$$B = -2I_s \alpha_2 Q_e \quad (35b)$$

$$C = I_s \alpha_2 Q_e^2 - P_1 + P_2 \quad (35c)$$

Since  $Q_v$  must be real, we must have

$$B^2 - 4AC \geq 0 \quad (36)$$

As we are ignoring the compliance of the end cavities, the flow  $Q_e$  is related to the displacement  $x_v$  by

$$Q_e = A_v \dot{x}_v \quad (37)$$

From equations 28, 29, and 37 it follows that the driving force  $F_v$  on the second-stage valve spool is given by

$$F_v = (P_e - P_e') A_v = I_s \alpha_2 A_v (Q_v - A_v \dot{x}_v) \quad (38)$$

However,  $Q_v$  can be determined by solving the quadratic equation 33, given  $\dot{x}_v$  and hence  $Q_e$ . The quantities  $I_v$ ,  $I_s$ , and  $I_r$  are determined so that the conditions 26, 30, and 36 are satisfied. Thus, we have shown that

$$F_v = f(x_v, \dot{x}_v, t) \quad (39)$$

### 3.2 SECOND-STAGE VALVE

The second-stage valve is pictured in figure 18. The valve spool is shown in the neutral position ( $x_{vs} = 0$ ). The overlap between the valve spool and the valve sleeve on each side of the drive cavity opening when the valve spool is in the neutral position is called the valve overlap (wol).

The equations describing the flow through the supply (return) port of the valve into the drive cavity are different when the supply (return) port is open and when it is closed. When the supply (return) port is open, the flow at low frequencies is given approximately by the flow through an orifice whose area is changing slowly with time. It is shown in a previous paper [1, Appendix D] that the pressure drop across the open supply port is given by

$$P_1 - P_2 = \frac{\rho_h Q_s |Q_s|}{2 \eta^2 A_{sp}^2} \quad (40)$$

where  $P_1$  is the pressure on the upstream side of the supply port,  $P_2$  is the pressure on the drive cavity side of the supply port,  $A_{sp}$  is the area of the supply port opening, and

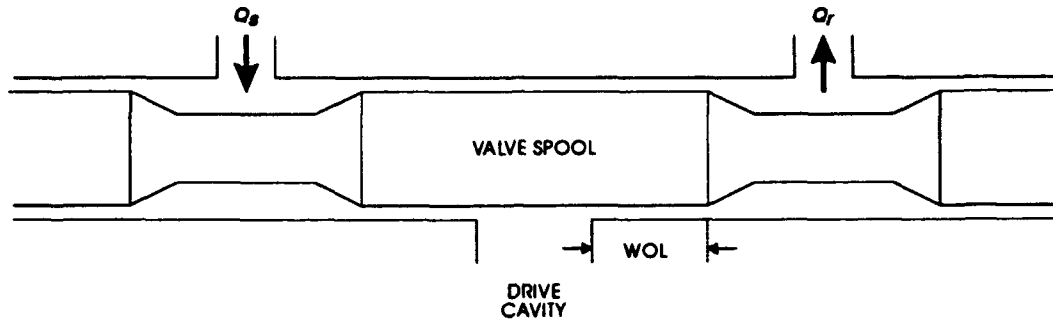


Figure 18. Second-stage valve.

$\eta$  is the ratio of the flow stream area at the point of greatest contraction to the valve opening area. The pressure  $P_1$  is different from the supply pressure  $P_s$  since there are passages and fittings between the pump and the valve. Similarly, the pressure drop across the return port when it is open is given by

$$P_2 - P_3 = \frac{\rho_h Q_r |Q_r|}{2 \eta^2 A_{rp}^2} \quad (41)$$

where  $P_3$  is the pressure on the downstream side of the return port and  $A_{rp}$  is the area of the return port opening.

We next derive expressions for the areas  $A_{sp}$ ,  $A_{rp}$  as a function of valve position. The supply port opening is pictured in figure 19. The rounded corners shown on the valve sleeve and the valve spool are greatly exaggerated (rad=0.002 in.). When the supply port is open we have

$$x_v = \sqrt{(x_{vs} - wol + 2 \cdot rad)^2 + (rcl + 2 \cdot rad)^2} - 2 \cdot rad \quad (42)$$

where  $x_{vs}$  is the displacement of the valve from neutral position (a positive increase in  $x_{vs}$  tends to open the supply port). The area  $A_{sp}$  of the supply port opening is given approximately by

$$A_{sp} \doteq \pi D_v x_v \quad (rcl \ll D_v) \quad (43)$$

where  $D_v$  is the diameter of the valve spool.

Similarly, when the return port is open we have

$$x_v = \sqrt{(-x_{vs} - wol + 2 \cdot rad)^2 + (rcl + 2 \cdot rad)^2} - 2 \cdot rad \quad (44)$$

and

$$A_{rp} \doteq \pi D_v x_v \quad (rcl \ll D_v). \quad (45)$$

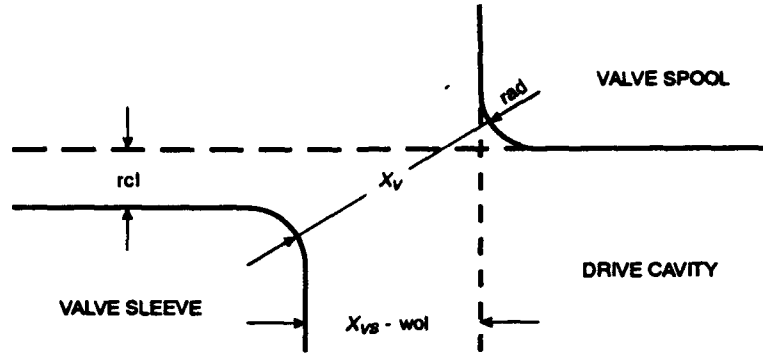


Figure 19. Supply port geometry.

Combining equations 40 and 43 results in

$$P_1 - P_2 = \frac{\rho_h}{2} \frac{Q_s |Q_s|}{\eta^2 \pi^2 D_v^2 x_v^2} \quad (46)$$

Similarly, combining equations 41 and 45 results in

$$P_2 - P_3 = \frac{\rho_h}{2} \frac{Q_r |Q_r|}{\eta^2 \pi^2 D_v^2 x_v^2} \quad (47)$$

The pressure drops  $P_s - P_1$  and  $P_2 - P_D$  are given by

$$P_s - P_1 = L_s \dot{Q}_s + \frac{\rho_h Q_s |Q_s|}{2\eta^2 A_s^2} \quad (48)$$

and

$$P_2 - P_D = L_{so} \dot{Q}_s + \frac{\rho_h Q_s |Q_s|}{2\eta^2 A_{so}^2} \quad (49)$$

where  $L_s$  is the supply flow path inertance,  $L_{so}$  is the supply output flow path inertance,  $A_s$  is the supply flow path equivalent area, and  $A_{so}$  is the supply output flow path equivalent area. The pressure drops  $P_D - P_2$  and  $P_3 - P_r$  are given by

$$P_3 - P_r = L_r \dot{Q}_r + \frac{\rho_h Q_r |Q_r|}{2\eta^2 A_r^2} \quad (50)$$

and

$$P_D - P_2 = L_{ro} \dot{Q}_r + \frac{\rho_h Q_r |Q_r|}{2\eta^2 A_{ro}^2} \quad (51)$$

where  $L_r$  is the return flow path inertance,  $L_{ro}$  is the return output flow path inertance,  $A_r$  is the return flow path equivalent area, and  $A_{ro}$  is the return output flow path equivalent area.

Combining equations 40, 48, and 49 yields

$$(L_s + L_{so})\dot{Q}_s = P_s - P_D - \frac{\rho_h}{2\eta^2} \left( \frac{1}{A_s^2} + \frac{1}{A_{so}^2} + \frac{1}{\pi^2 D_v^2 x_v^2} \right) Q_s |Q_s| \quad (52)$$

when the supply port is open. Similarly

$$(L_r + L_{ro})\dot{Q}_r = P_D - P_r - \frac{\rho_h}{2\eta^2} \left( \frac{1}{A_r^2} + \frac{1}{A_{ro}^2} + \frac{1}{\pi^2 D_v^2 x_v^2} \right) Q_r |Q_r| \quad (53)$$

when the return port is open.

When the supply port is closed the leakage flow is given by [1,p.15]:

$$Q_s = \text{sgn}(P_s - P_D) \left[ -\frac{1}{2}k_0^2 R_L + \sqrt{\frac{1}{2}k_0^2 R_L + k_0^2 |P_s - P_D|} \right] \quad (54)$$

where

$$R_L = \frac{12\mu x_L}{\pi D_v (\text{rcl})^3}, \quad k_0^2 = \frac{2\eta^2 \pi^2 D_v^2 (\text{rcl})^2}{\rho_h}, \quad x_L = \text{wol} - x_{vs} \quad (55)$$

and  $\mu$  is the shear viscosity coefficient of the fluid. Similarly, when the return port is closed

$$Q_r = \text{sgn}(P_D - P_r) \left[ -\frac{1}{2}k_0^2 R_L + \sqrt{\frac{1}{2}k_0^2 R_L + k_0^2 |P_D - P_r|} \right] \quad (56)$$

where now  $x_L = x_{vs} + \text{wol}$ .

The equation of motion for the second-stage valve spool can be written in the form

$$M_{vs} \ddot{x}_{vs} + 2K_s x_{vs} = F_v + F_{flow} \quad (57)$$

or equivalently

$$\dot{x}_{vs} = \frac{1}{M_{vs}} (F_v + F_{flow} - 2K_s x_{vs}) \quad (58a)$$

$$\dot{x}_{vs} = v_{vs} \quad (58b)$$

where  $x_{vs}$  is the lineal valve displacement,  $M_{vs}$  is the mass of the valve spool,  $K_s$  is the stiffness of each of the two restraining springs,  $F_v$  is the driving force on the spool given in equation 33, and  $F_{flow}$  is the axial force on the spool due to the flow through the valve. The force  $F_{flow}$  is given approximately by [5]:

$$F_{flow} = -\text{sgn}(x_{vs}) \rho_h Q U \cos \theta \quad (59)$$

where  $\rho_h$  is the density of the hydraulic fluid,  $Q$  is the flow through the valve (supply or return),  $U$  is the velocity of the jet at the point of maximum contraction (*vena contracta*),

and  $\cos \theta \doteq 0.36$  ( $\theta$  is the angle of the flow relative to the axis). Since  $Q = \eta UA$ , where  $A$  is the area of the valve opening, equation 59 can be written

$$F_{flow} = -0.36 \operatorname{sgn}(x_{vs}) \frac{\rho_h Q^2}{\eta A} \quad (60)$$

The area of the valve opening is given approximately by

$$A \doteq \pi D_v x_v \quad (61)$$

Thus, equation 60 can be written

$$F_{flow} = -0.36 \operatorname{sgn}(x_{vs}) \frac{\rho_h Q^2}{\eta \pi D_v x_v} \quad (62)$$

Since the flow through the closed port is small, we can write approximately

$$F_{flow} \doteq -0.36 \operatorname{sgn}(x_{vs}) \frac{\rho_h (Q_r^2 + Q_s^2)}{\eta \pi D_v x_v} \quad (63)$$

### 3.3 PRESSURE COMPENSATION

In order to allow the transducer to operate at large depths the interior of the transducer is filled with a pressurized gas. The pressure of the gas is adjusted to be equal to the hydrostatic pressure in the water at the operating depth. Thus, the pressure  $P_0$  of the interior gas is adjusted so that

$$P_0 = P_{atm} + \rho g D \quad (64)$$

where  $P_{atm}$  is atmospheric pressure,  $\rho$  is the density of the water,  $g$  is the acceleration of gravity, and  $D$  is the operating depth.

In addition to providing depth compensation, the pressurized gas also presents a dynamic stiffness to each of the radiating disks. By symmetry it is only necessary to consider one of the radiating disks and half of the interior volume. When the disk vibrates the interior volume changes which in turn produces a change in pressure. It will be assumed that the pressurized gas obeys the ideal gas law

$$PV^\gamma = P_0 V_0^\gamma \quad \gamma = 1.4 \quad (65)$$

where  $\gamma$  is the adiabatic gas constant,  $P$  is the pressure,  $V$  is the volume of gas,  $P_0$  is the initial pressure charge, and  $V_0$  is the initial volume of gas. Let  $\tilde{P}$  and  $\tilde{V}$  be the changes in pressure and volume produced by the vibration of the disk, i.e.

$$P = P_0 + \tilde{P} \quad V = V_0 + \tilde{V} \quad (66)$$

Combining equations 65 and 66, we obtain

$$\left(1 + \frac{\tilde{P}}{P_0}\right) \left(1 + \frac{\tilde{V}}{V_0}\right)^\gamma = 1 \quad (67)$$

Assuming that  $\tilde{P} \ll P_0$  and  $\tilde{V} \ll V_0$ , it follows from equation 67 that

$$\left(1 + \frac{\tilde{P}}{P_0}\right) \left(1 + \gamma \frac{\tilde{V}}{V_0}\right) \doteq 1 \quad (68)$$

or

$$\tilde{P} \doteq -\gamma \frac{P_0}{V_0} \tilde{V} \quad (69)$$

If  $u$  is the normal displacement of the disk, then the volume change  $\tilde{V}$  is given by

$$\tilde{V} = \int_A u \, dA \quad (70)$$

The displacement  $u$  can be approximated by

$$u = u_1 \phi_1 + u_2 \phi_2 + u_3 \phi_3 + u_4 \phi_4 \quad (71)$$

where  $\phi_1, \phi_2, \phi_3,$  and  $\phi_4$  are the dominant mode shapes of the disk (normalized to be unity at the disk center). Combining equations 69-71, we obtain

$$\begin{aligned} \tilde{P} &\doteq -\gamma \frac{P_0}{V_0} \sum_{n=1}^4 u_n \int_A \phi_n \, dA \\ &= -\gamma \frac{P_0 A}{V_0} \sum_{n=1}^4 \alpha_n u_n \end{aligned} \quad (72)$$

where  $\alpha_n$  is defined by

$$\alpha_n = \frac{1}{A} \int_A \phi_n \, dA \quad (73)$$

The finite-element modal force component  $F_m$  is given by

$$F_m = \int_A \tilde{P} \phi_m \, dA \doteq \tilde{P} A \alpha_m \quad (74)$$

Thus

$$\begin{aligned} F_m &= -\frac{\gamma P_0 A^2}{V_0} \sum_{n=1}^4 \alpha_m \alpha_n u_n \\ &= -\sum_{n=1}^4 \hat{K}_{mn} u_n \end{aligned} \quad (75)$$

where

$$\hat{K}_{mn} = \frac{\gamma P_0 A^2}{V_0} \alpha_m \alpha_n \quad (76)$$

Let  $\beta$  be the fraction of the interior volume that is filled with gas. Then

$$V_0 = \beta Ah \quad (77)$$

where  $A$  is the area of the disk and  $h$  is the half height of the cylindrical housing. Substituting equation 77 into equation 76, we get

$$\hat{K}_{mn} = \frac{\gamma P_0 A}{\beta h} \alpha_m \alpha_n \quad (78)$$

Equation 75 is the desired dynamic stiffness relation.

### 3.4 RADIATING DISKS AND DRIVE CAVITY

The radiating disks were modeled by using the finite-element method. Four symmetric modes were used to represent the motion of the disks. The modes were normalized so that the normal component of displacement at the disk center was unity. In terms of these modes the equation of motion for the  $m$ -th element can be written

$$M_i \ddot{u}_m^i(t) + K_i u_m^i(t) = P_m(t) A_p - F_m^i(t) \quad i = 1, 2, 3, 4 \quad (79)$$

where  $M_i$  is the modal mass of the  $i$ -th mode,  $K_i$  is the modal stiffness of the  $i$ -th mode,  $u_m^i$  is the  $i$ -th modal displacement of the  $m$ -th element,  $P_m$  is the drive cavity pressure of the  $m$ -th element,  $A_p$  is the area of the drive piston, and  $F_m^i$  is the  $i$ -th modal component of the acoustic radiation force on the  $m$ -th element. This equation can be written in the alternative form

$$M_i a_m^i(t) + K_i u_m^i(t) = P_m(t) A_p - F_m^i(t) \quad (80a)$$

$$\dot{v}_m^i(t) = \dot{a}_m^i(t) \quad (80b)$$

$$\dot{u}_m^i(t) = v_m^i(t) \quad i = 1, 2, 3, 4 \quad (80c)$$

Equation 7 for the radiation force in the linear model can be extended to this problem as follows:

$$F_m^i(t) = \sum_{j=1}^4 \sum_{n=1}^N \int_0^t \mu_{mn}^{ij}(\tau) a_n^j(t - \tau) d\tau \quad i = 1, 2, 3, 4 \quad (81)$$

Combining equations 80 and 81, we obtain

$$M_i a_m^i(t) + K_i u_m^i(t) = P_m(t) A_p - \sum_{j=1}^4 \hat{K}_{ij} u_m^j(t) - \sum_{j=1}^4 \sum_{n=1}^N \int_0^t \mu_{mn}^{ij}(\tau) a_n^j(t - \tau) d\tau \quad (82a)$$

$$\dot{v}_m^i(t) = \dot{a}_m^i(t) \quad (82b)$$

$$\dot{u}_m^i(t) = v_m^i(t) \quad i = 1, 2, 3, 4 \quad (82c)$$

In order to solve the differential-integral equations for this problem, we will rewrite equations 82 as was done in the linear problem. Let  $t$  be in the interval  $t_r < t \leq t_{r+1}$ . Then the integrals on the right-hand side of equation 82 can be split as follows:

$$\int_0^t \mu_{mn}^{ij}(\tau) a_n^j(t-\tau) d\tau = \int_0^{t-t_r} \mu_{mn}^{ij}(\tau) a_n^j(t-\tau) d\tau + \int_{t-t_r}^t \mu_{mn}^{ij}(\tau) a_n^j(t-\tau) d\tau \quad (83)$$

Since an element does not feel the effects of its neighboring elements immediately, it follows that

$$\int_0^{t-t_r} \mu_{mn}^{ij}(\tau) a_n^j(t-\tau) d\tau = 0 \quad m \neq n \quad (84)$$

When  $m = n$  the first integral in equation 83 can be approximated by using the trapezoidal rule as follows:

$$\int_0^{t-t_r} \mu_{mm}^{ij}(\tau) a_m^j(t-\tau) d\tau \doteq \left(\frac{t-t_r}{2}\right) [\mu_{mm}^{ij}(0) a_m^j(t) + \mu_{mm}^{ij}(t-t_r) a_m^j(t_r)] \quad (85)$$

Inserting equations 83-85 into equation 82 yields

$$\begin{aligned} M_i a_m^i(t) + \left(\frac{t-t_r}{2}\right) \sum_{j=1}^4 \mu_{mm}^{ij}(0) a_m^j(t) &= P_m(t) A_p - K_i u_m^i(t) - \sum_{j=1}^4 \hat{K}_{ij} u_m^j(t) - \\ &\sum_{j=1}^4 \sum_{n=1}^N \int_{t-t_r}^t \mu_{mn}^{ij}(\tau) a_n^j(t-\tau) d\tau - \\ &\left(\frac{t-t_r}{2}\right) \sum_{j=1}^4 \mu_{mm}^{ij}(t-t_r) a_m^j(t_r) \end{aligned} \quad (86a)$$

$$\dot{v}_m^i(t) = a_m^i(t) \quad (86b)$$

$$\dot{u}_m^i(t) = v_m^i(t) \quad i = 1, 2, 3, 4 \quad (86c)$$

The three equations in 86 can be solved for the  $a_m^i$  in terms of the remaining variables.

The pressure  $P_m$  in the drive cavity satisfies the equation

$$C \dot{P}_m(t) = \text{net flow into the cavity} = Q_m^{\text{in}}(t) - A_p v_m^{\text{cen}}(t) \quad (87)$$

where  $C$  is the compliance of the cavity,  $v_m^{\text{cen}}$  is the center velocity of element  $m$ , and  $Q_m^{\text{in}}$  is the flow into the drive cavity of the  $m$ -th element through the second-stage valve. Since the modes were normalized to unity at the center, the velocity  $v_m^{\text{cen}}$  can be written

$$v_m^{\text{cen}}(t) = \sum_{i=1}^4 v_m^i(t) \quad (88)$$

The net flow  $Q_m^{\text{in}}$  is given by

$$Q_m^{\text{in}}(t) = Q_m^s(t) - Q_m^r(t) \quad (89)$$

where  $Q_m^s$  and  $Q_m^r$  are the supply and return flows for the  $m$ -th element. Substituting equations 88 and 89 into equation 87 produces

$$\dot{P}_m(t) = \frac{1}{C} \left[ Q_m^s(t) - Q_m^r(t) - A_p \sum_{i=1}^4 v_m^i(t) \right] \quad (90)$$

### 3.5 SUMMARY OF EQUATIONS

In this subsection we will present a summary of the differential-integral equations for a hydroacoustic array obtained in previous subsections. The equations will be given for the  $m$ -th element of an array. There will be a system of equations like this for each element in the array.

**Radiating disk equations:**

$$\begin{aligned}\dot{v}_m^i &= a_m^i \\ \dot{u}_m^i &= v_m^i \quad i = 1, 2, 3, 4\end{aligned}$$

where

$$M_i a_m^i + K_i u_m^i = P_m A_p - \sum_{j=1}^4 \hat{K}_{ij} u_m^j - \sum_{j=1}^4 \sum_{n=1}^N \int_0^t \mu_{mn}^{ij}(\tau) a_n^j(t - \tau) d\tau$$

**Drive cavity equation:**

$$\dot{P}_m = \frac{1}{C} \left[ Q_m^s - Q_m^r - A_p \sum_{i=1}^4 v_m^i \right]$$

**Valve spool equations:**

$$\begin{aligned}\dot{x}_{vs} &= \frac{1}{M_{vs}} (F_v + F_{flow} - 2K_s x_{vs}) \\ \dot{x}_{vs} &= v_{vs}\end{aligned}$$

where

$$\begin{aligned}F_v &= f(x_v, \dot{x}_v, t) \\ F_{flow} &\doteq -0.36 \operatorname{sgn}(x_{vs}) \frac{\rho_h (Q_r^2 + Q_s^2)}{\eta \pi D_v x_v}\end{aligned}$$

**Valve flow equations:**

$$(L_s + L_{so}) \dot{Q}_s = P_s - P_D - \frac{\rho_h}{2\eta^2} \left( \frac{1}{A_s^2} + \frac{1}{A_{so}^2} + \frac{1}{\pi^2 D_v^2 x_v^2} \right) Q_s |Q_s| \quad \text{supply port open}$$

$$(L_r + L_{r0})\dot{Q}_r = P_D - P_r - \frac{\rho_h}{2\eta^2} \left( \frac{1}{A_r^2} + \frac{1}{A_{r0}^2} + \frac{1}{\pi^2 D_0^2 x_0^2} \right) Q_r |Q_r| \quad \text{return port open}$$

$$Q_s = \text{sgn}(P_s - P_D) \left[ -\frac{1}{2}k_0^2 R_L + \sqrt{\frac{1}{2}k_0^2 R_L + k_0^2 |P_s - P_D|} \right] \quad \text{supply port leakage}$$

$$Q_r = \text{sgn}(P_D - P_r) \left[ -\frac{1}{2}k_0^2 R_L + \sqrt{\frac{1}{2}k_0^2 R_L + k_0^2 |P_D - P_r|} \right] \quad \text{return port leakage}$$

The initial conditions for  $u_m^i$  and  $v_m^i$  ( $i = 1, 2, 3, 4$ ),  $x_{vs}$ ,  $v_{vs}$ ,  $Q_m^s$ , and  $Q_m^r$  are taken to be zero. The initial condition on the drive cavity pressure  $P_m$  is taken to be  $(P_s + P_r)/2$ . The solution procedure as outlined for the linear problem is applicable to the solution of this set of differential-integral equations.

### 3.6 RESULTS

This subsection contains computation results from the time-domain model for both single elements and arrays of HLF-6A transducers. The following normalizations have been employed in the figures:

1. Frequency has been shifted by a value designated as FL.
2. Time has been divided by  $s/c$ , where  $s$  is the diameter of an element and  $c$  is the sound speed.
3. All source levels have had the single-element target source level subtracted.
4. Array source levels also have had  $20 \log_{10}(N)$  subtracted, where  $N$  is the number of elements.
5. Velocities have been divided by the sound speed  $c$ .
6. Drive cavity pressures have been divided by the supply pressure.

Figures 20-23 show a comparison of results from the NRaD model and the HAI model for sinusoidal drives of four different levels and a number of different frequencies. At each drive frequency the fundamental component of the time response is plotted. A drive level of 0 dB corresponds to half the maximum displacement of the servovalve. For all drive

levels the agreement is quite good, but there are small differences (less than 1 dB) at the higher drive levels. HAI models the load (disk+pressure compensation+radiation) by a mass, stiffness, resistance, and shape factor for each drive frequency. The values of these parameters are chosen to match the drive point impedance at the drive frequency. This load is not correct at harmonics of the drive frequency produced by the nonlinearities of the device. In addition this approach is not applicable to nonsinusoidal drive signals. Figures 24-27 show the same comparison as above except that the NRaD model was modified to use the HAI loads. For all drive levels the results are virtually identical. This leads us to believe that the differences in figures 20-23 are due to differences in the way the load was modeled.

The next eight figures contain comparisons related to the drive point impedance of the load. Figures 28 and 29 show a comparison of the magnitude and phase of the drive point impedance between the NRaD time-domain model and the NRaD frequency-domain model. In the time-domain model only the fundamental components were used to form the impedance. The agreement is quite good over the entire frequency band. Figures 30 and 31 show the same comparison for the HAI time-domain and frequency-domain models. Again the agreement is excellent. Figures 32 and 33 show a comparison of the drive point impedance magnitude and phase between the NRaD frequency-domain model and the HAI frequency-domain model. The agreement is excellent. Figures 34 and 35 show the same comparison for the time-domain models. Again the agreement is good. Since the NRaD and HAI models produce virtually the same drive point impedance at the load, it appears that any differences in results must be due to higher harmonics of the drive frequency.

The next four figures show results for a three-element line array in which the center-to-center spacing is twice the element diameter. Figure 36 shows a comparison of normalized source level computed with the NRaD time-domain model and the experimental results obtained at Lake Seneca by Naval Research Laboratory/Underwater Sound Reference Detachment (NRL/USRD).<sup>1</sup> The comparison is reasonably good both in levels and in trends, but there appears to be a small frequency shift in the peaks. Figure 37 shows a comparison of model results for a single element and for the three-element array. This comparison indicates that at this element spacing the array source level can not be obtained by adding  $20 \log_{10}(3)$  to the single-element source level. Figures 38 and 39 show the time response of the center velocity and drive cavity pressure for the middle element of the three-element array. The fact that the transient behavior dies out very quickly is due to inherently high losses in the second-stage valve flow.

The next three figures are for a proposed six-element line array in which the center-to-center spacing is 9.26 times the element diameter. Figures 40 and 41 show a comparison of the time response of the center velocity and drive cavity pressure for a single element

---

<sup>1</sup>Data supplied by Steven Black of NRL/USRD in a private communication

versus a middle element of the six-element array. At this large element spacing the results are virtually identical. Figure 42 shows that the source level for this six-element array can be obtained by adding  $20 \log_{10}(6)$  to the single-element source level.

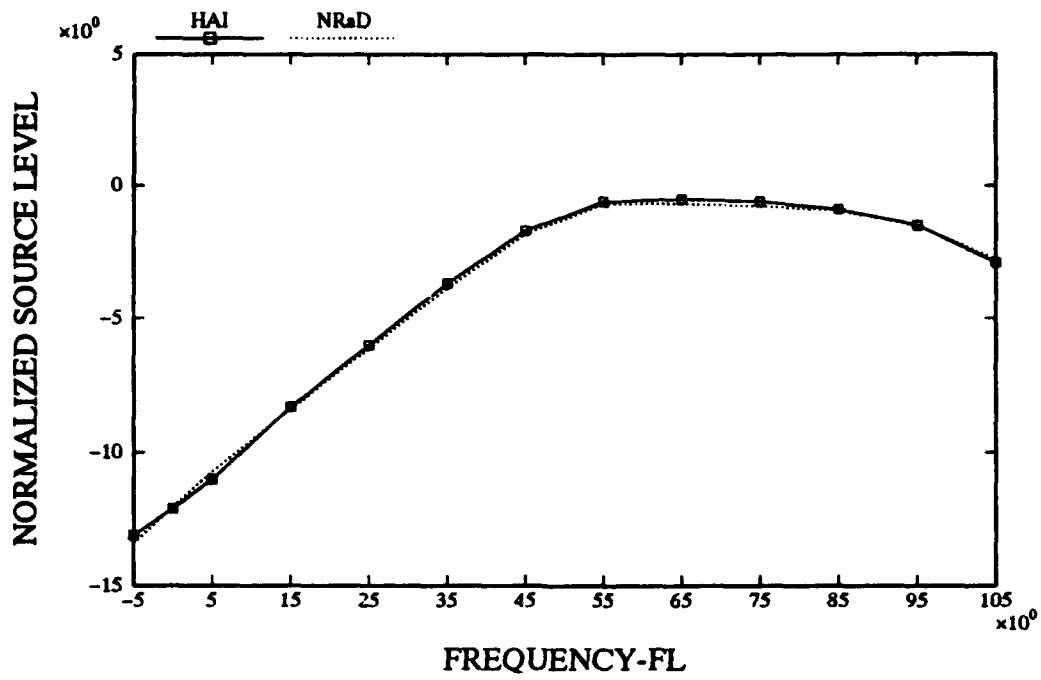


Figure 20. Single element, -6 dB drive level.

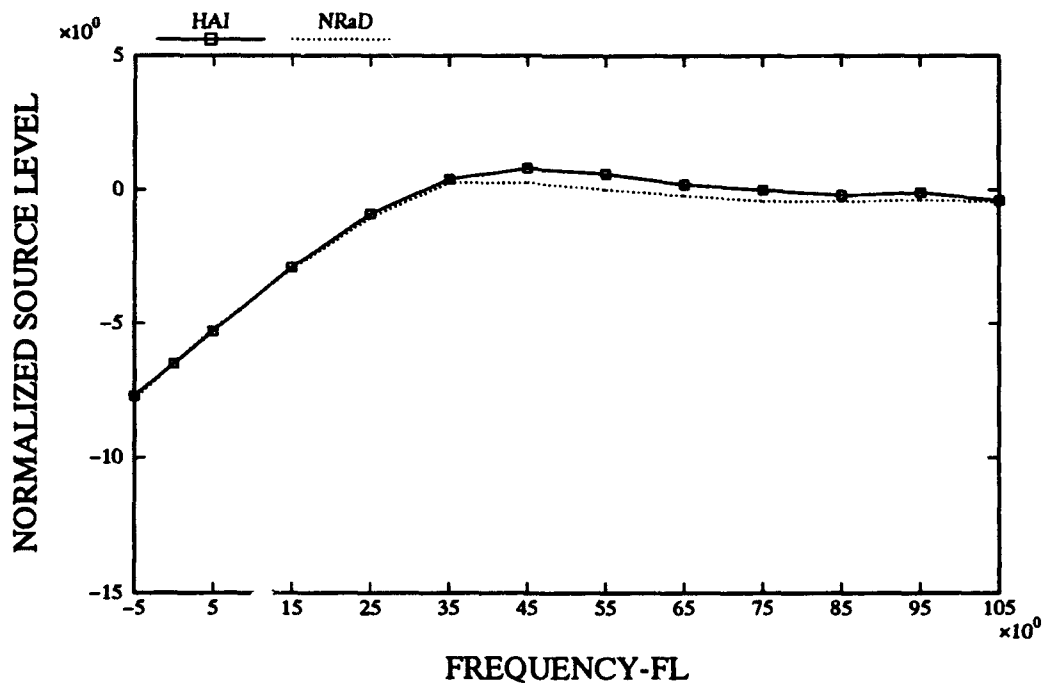


Figure 21. Single element, -3 dB drive level.

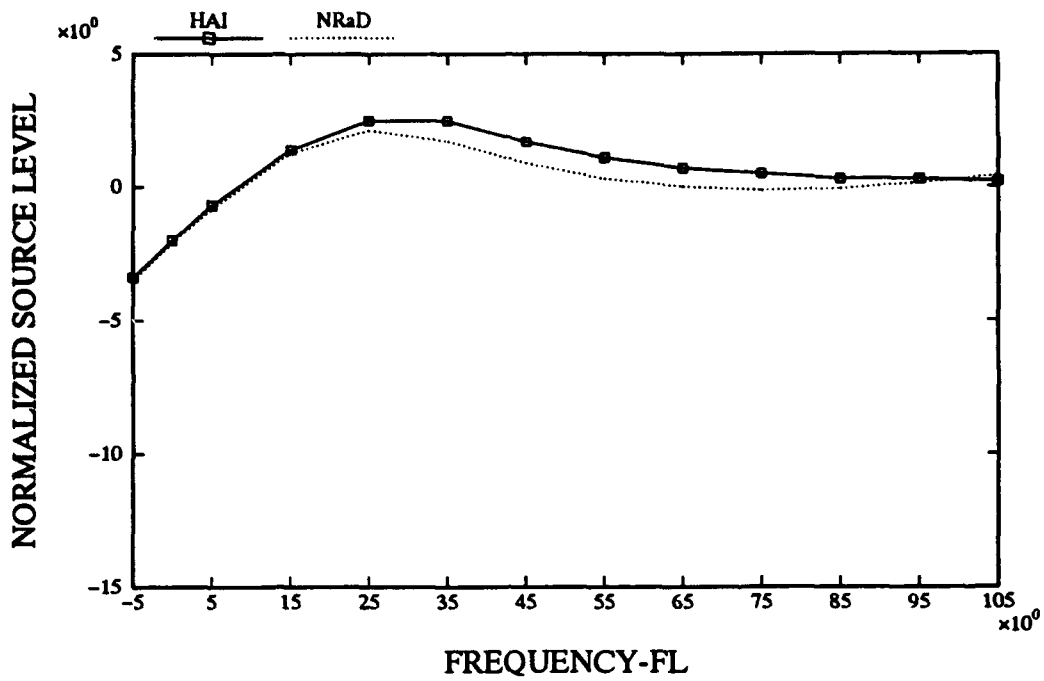


Figure 22. Single element, 0 dB drive level.

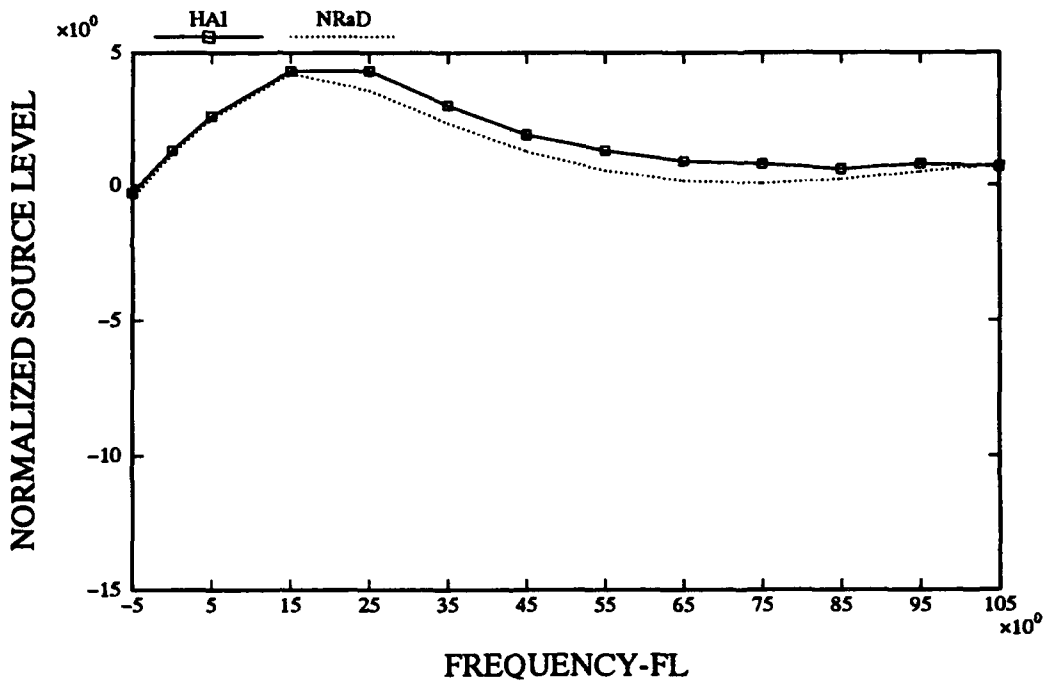


Figure 23. Single element, 3 dB drive level.

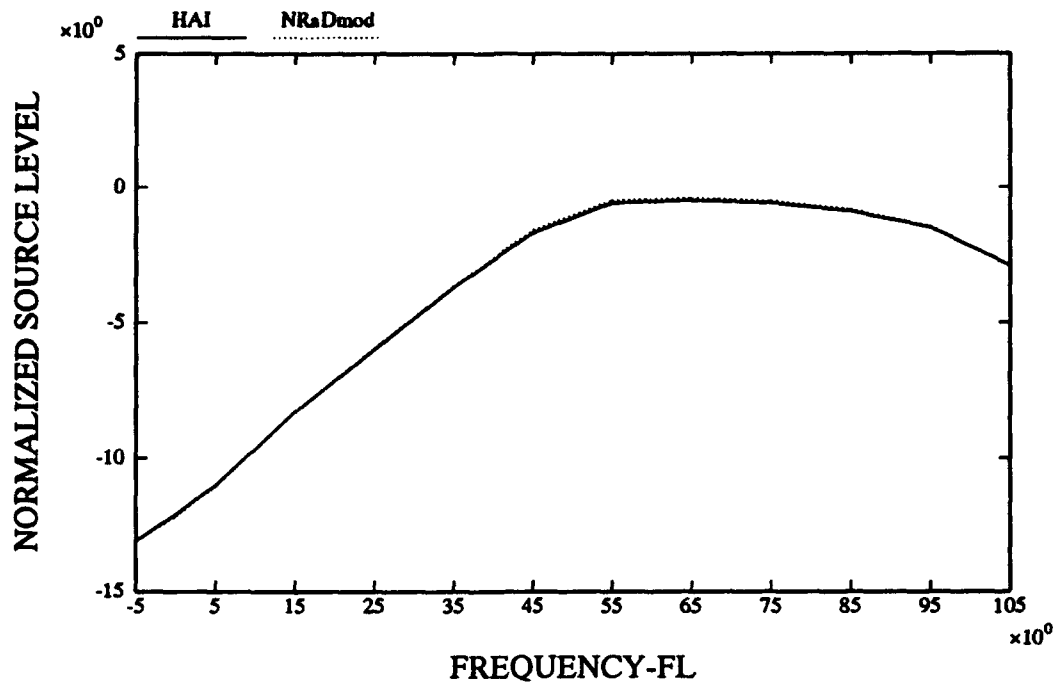


Figure 24. Single element, -6 dB drive level, HAI load model.

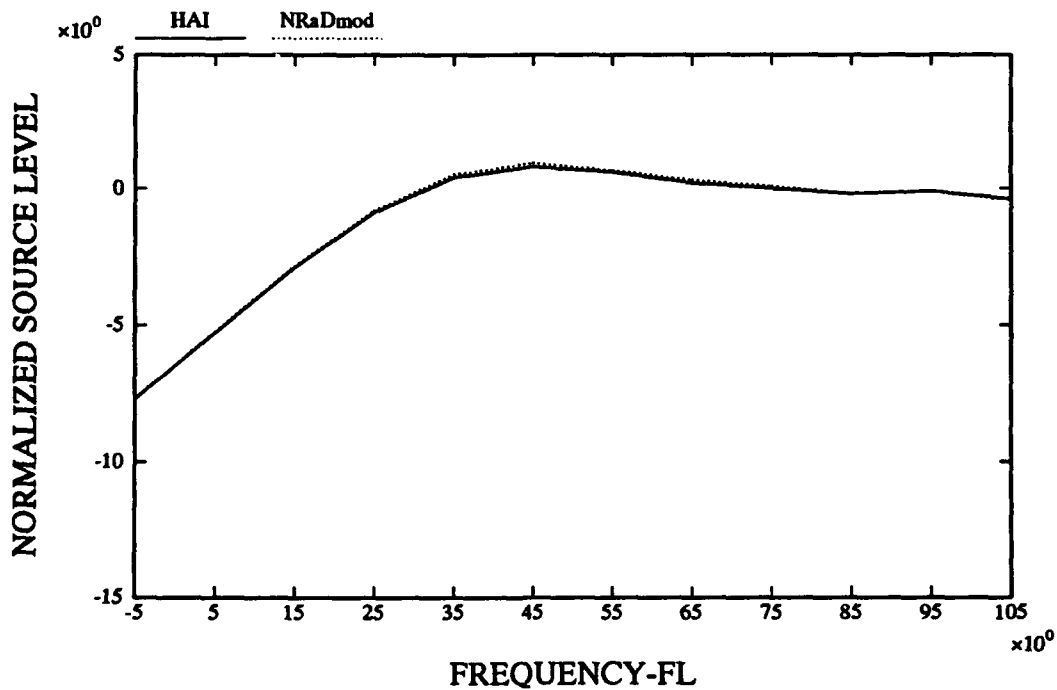


Figure 25. Single element, -3 dB drive level, HAI load model.

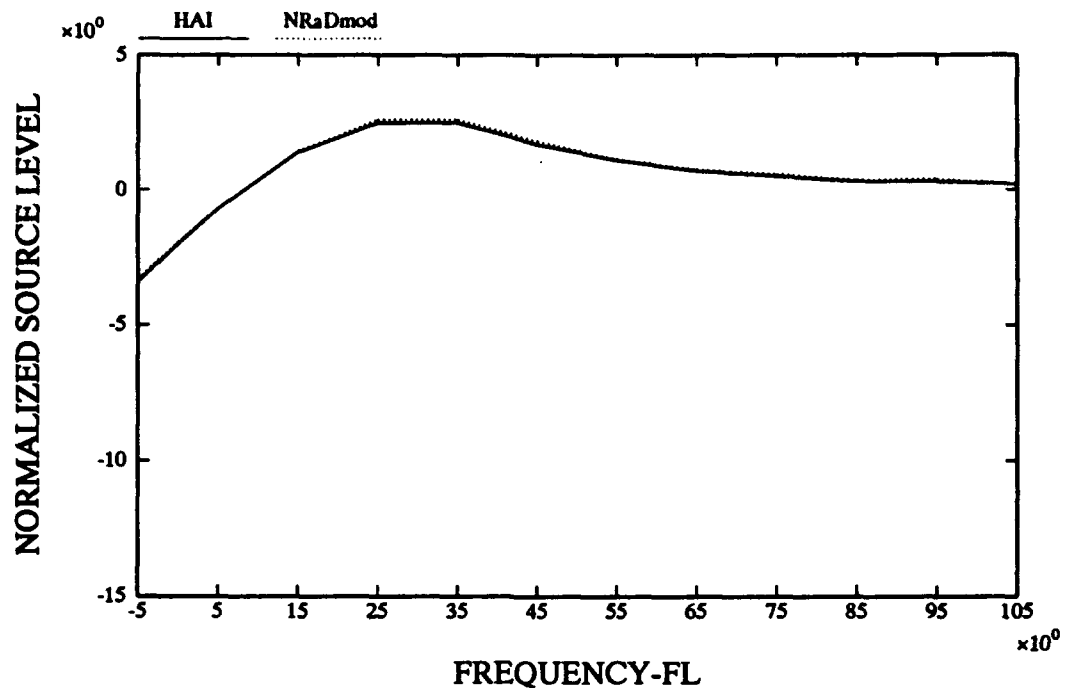


Figure 26. Single element, 0 dB drive level, HAI load model.

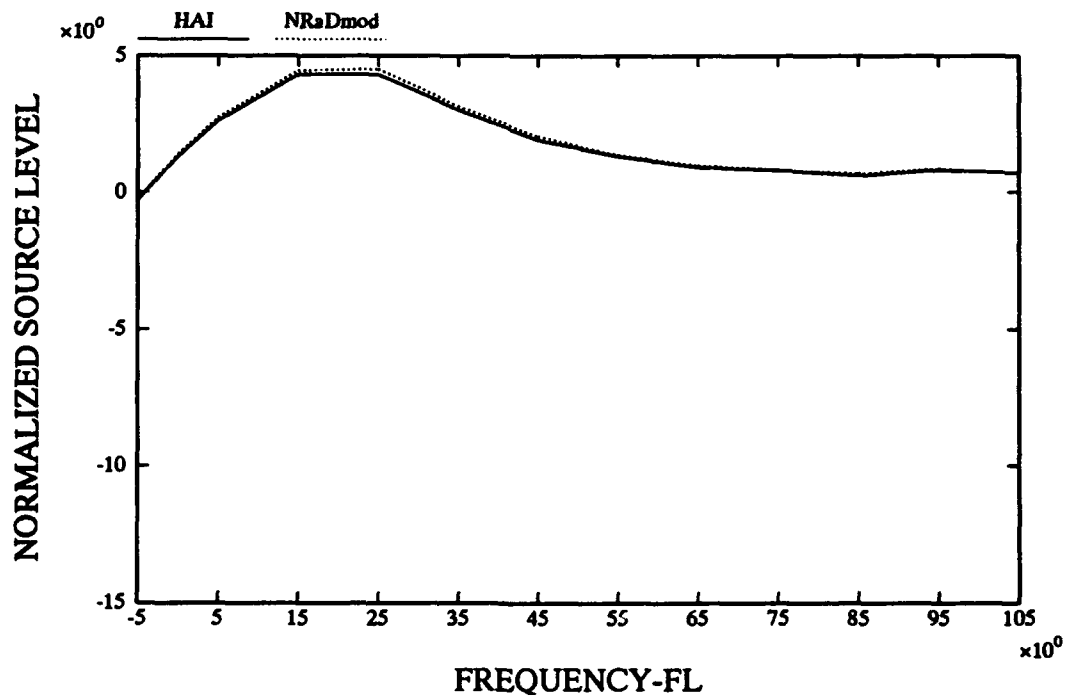


Figure 27. Single element, 3 dB drive level, HAI load model.

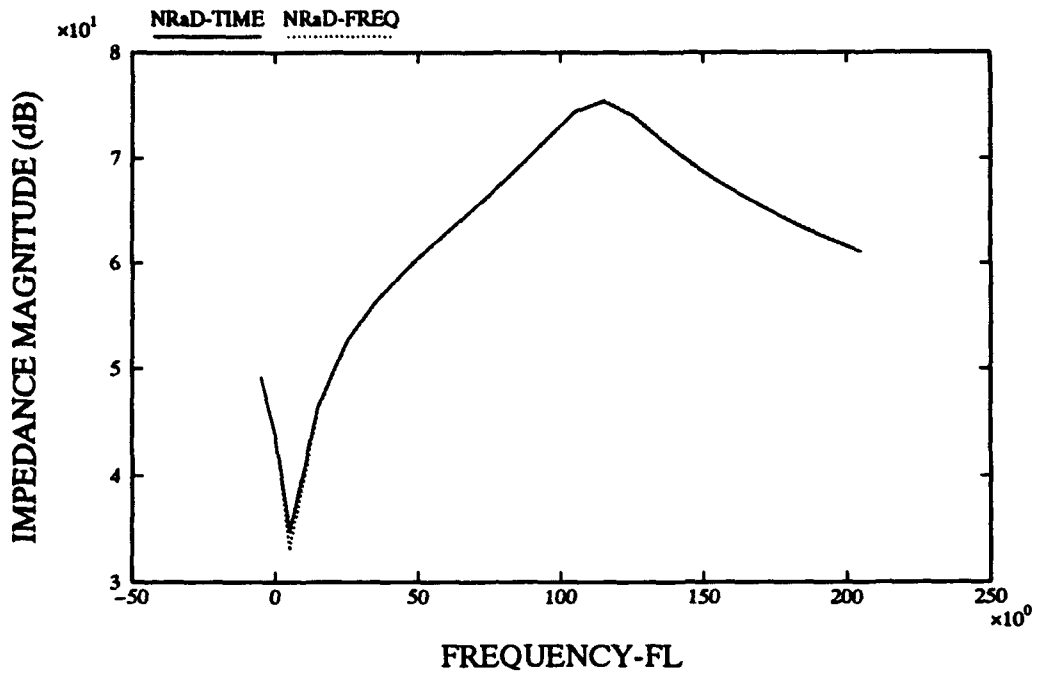


Figure 28. NRaD impedance magnitude comparison.

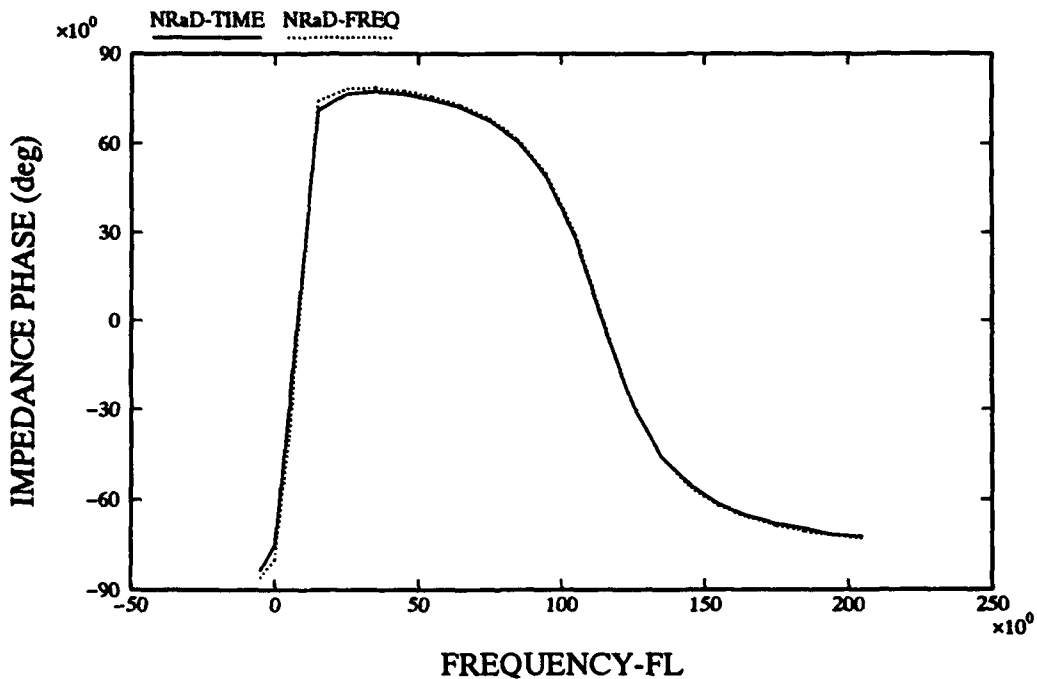


Figure 29. NRaD impedance phase comparison.

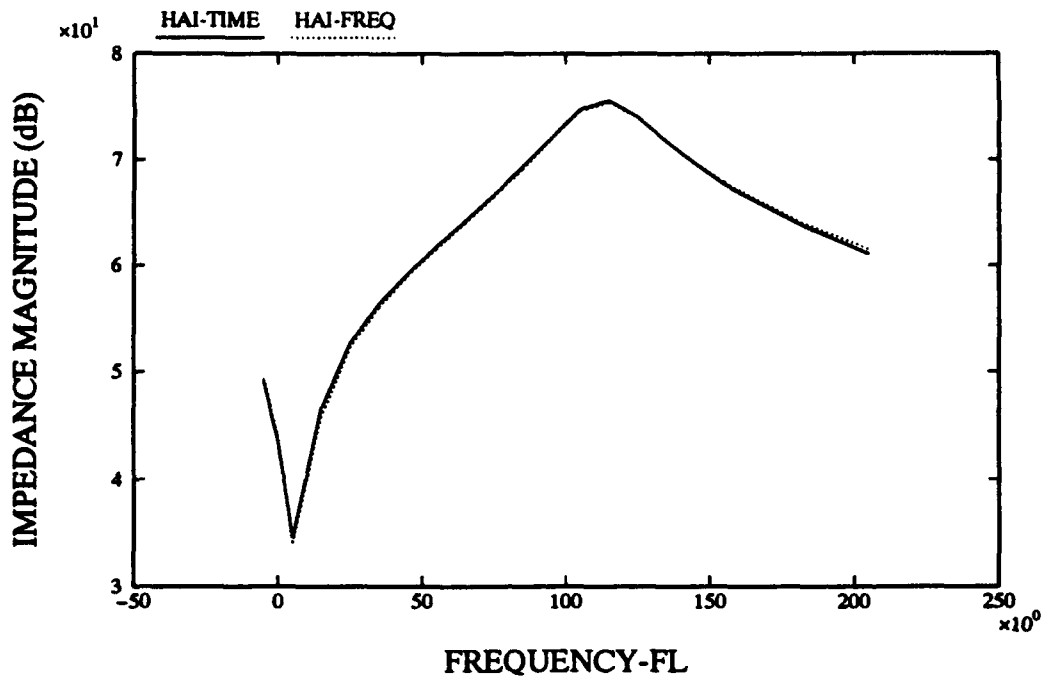


Figure 30. HAI impedance magnitude comparison.

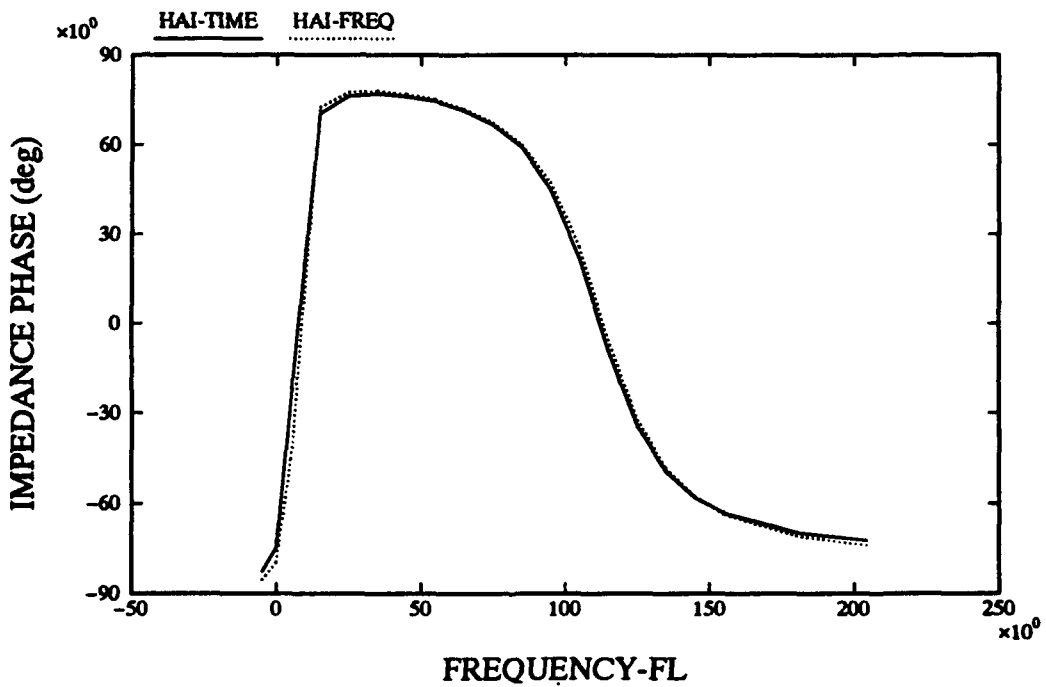


Figure 31. HAI impedance phase comparison.

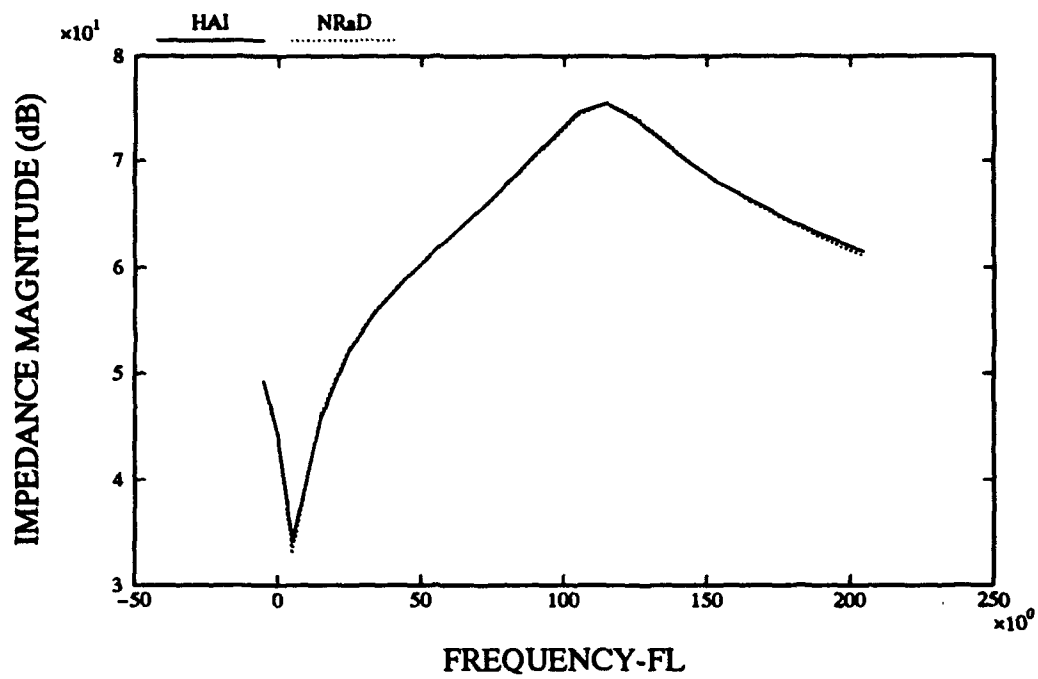


Figure 32. Impedance magnitude, NRaD vs HAI, frequency-domain model.

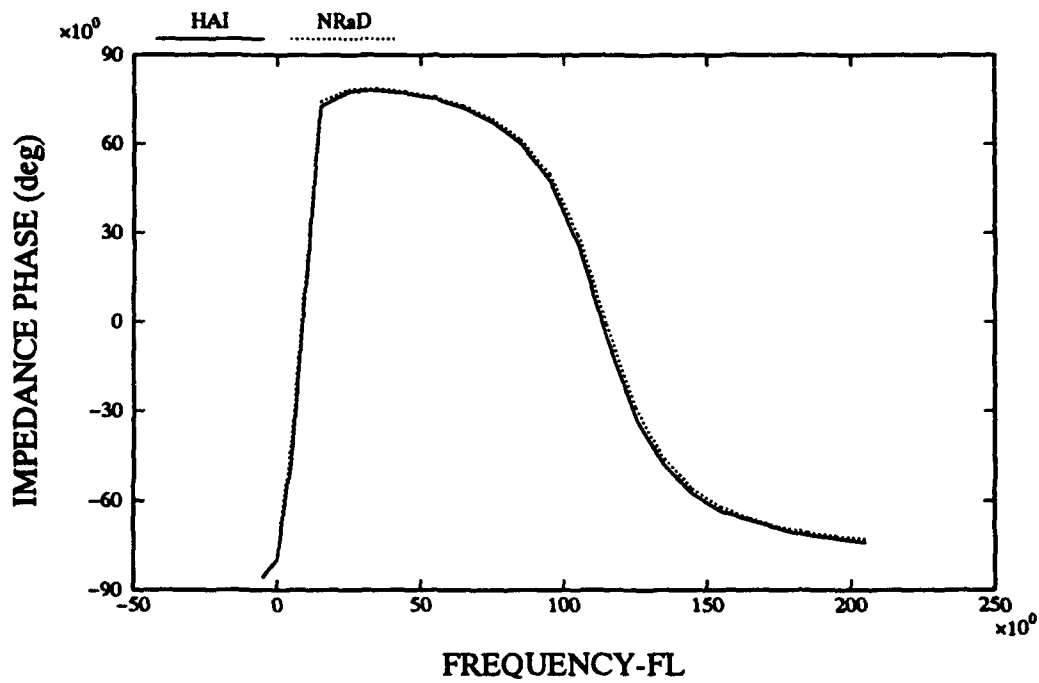


Figure 33. Impedance phase, NRaD vs HAI, frequency-domain model.

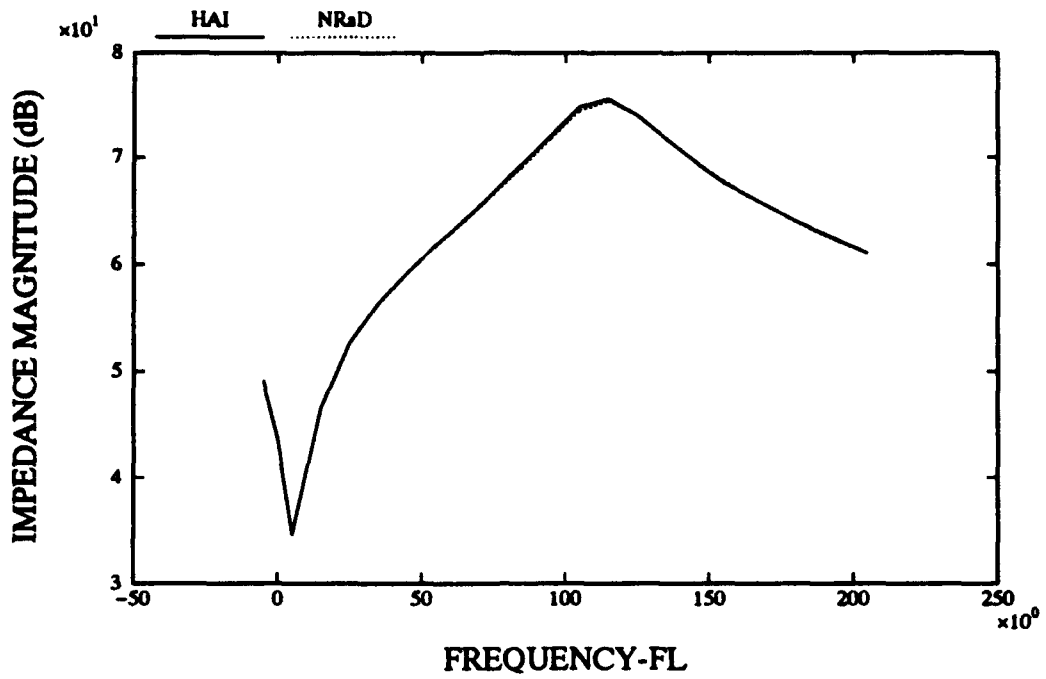


Figure 34. Impedance magnitude, NRaD vs HAI, time-domain model.

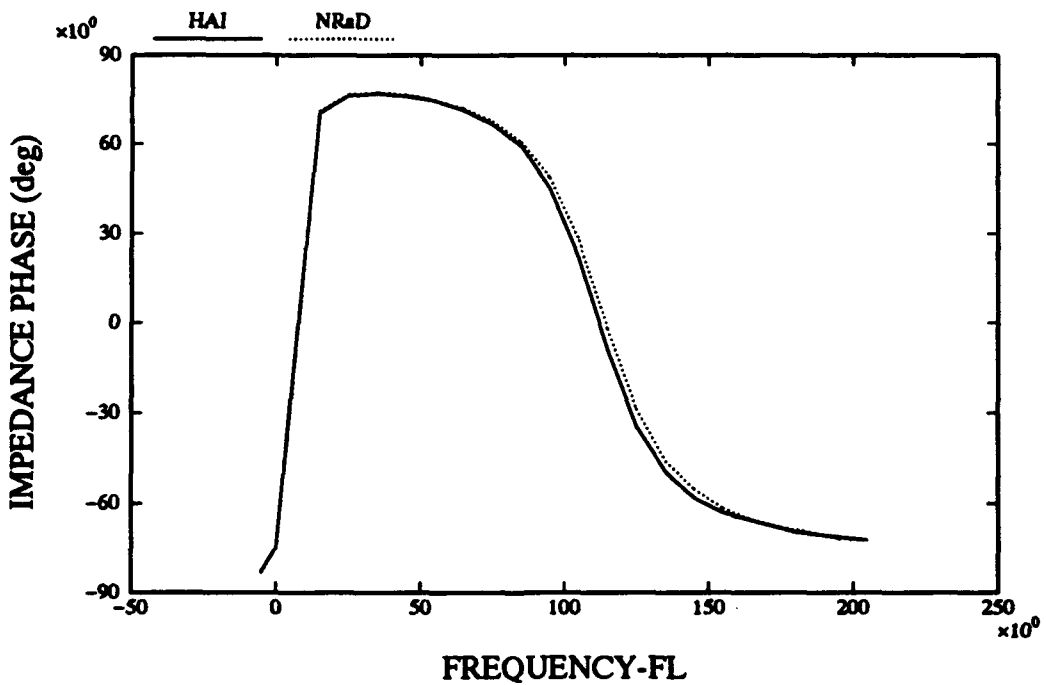


Figure 35. Impedance phase, NRaD vs HAI, time-domain model.

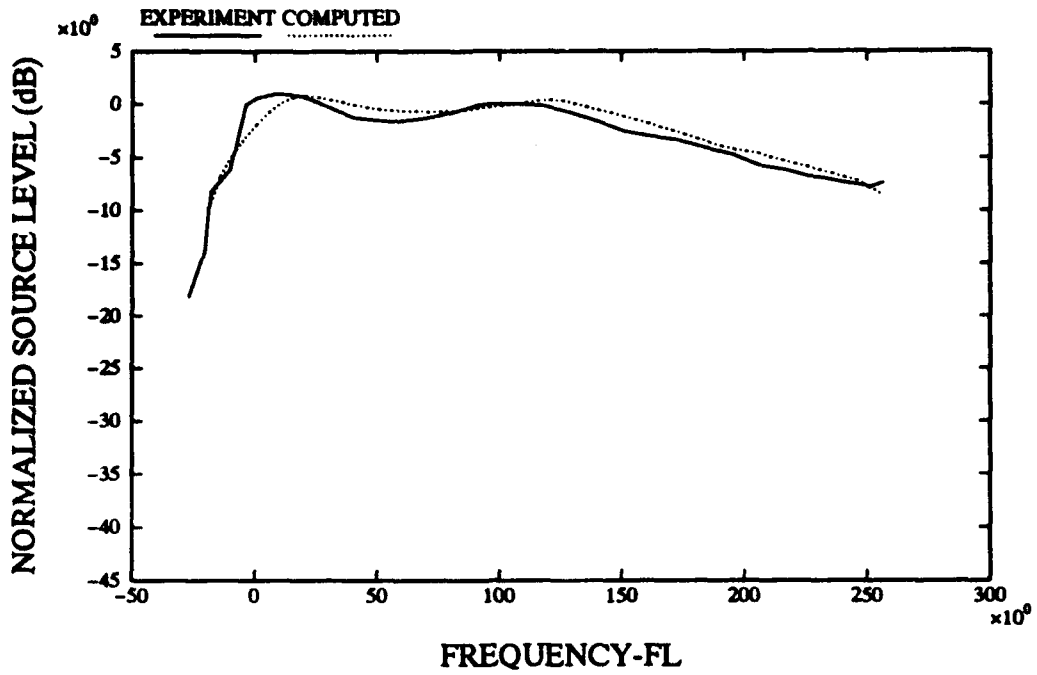


Figure 36. Source level for three-element array, experiment vs computed.

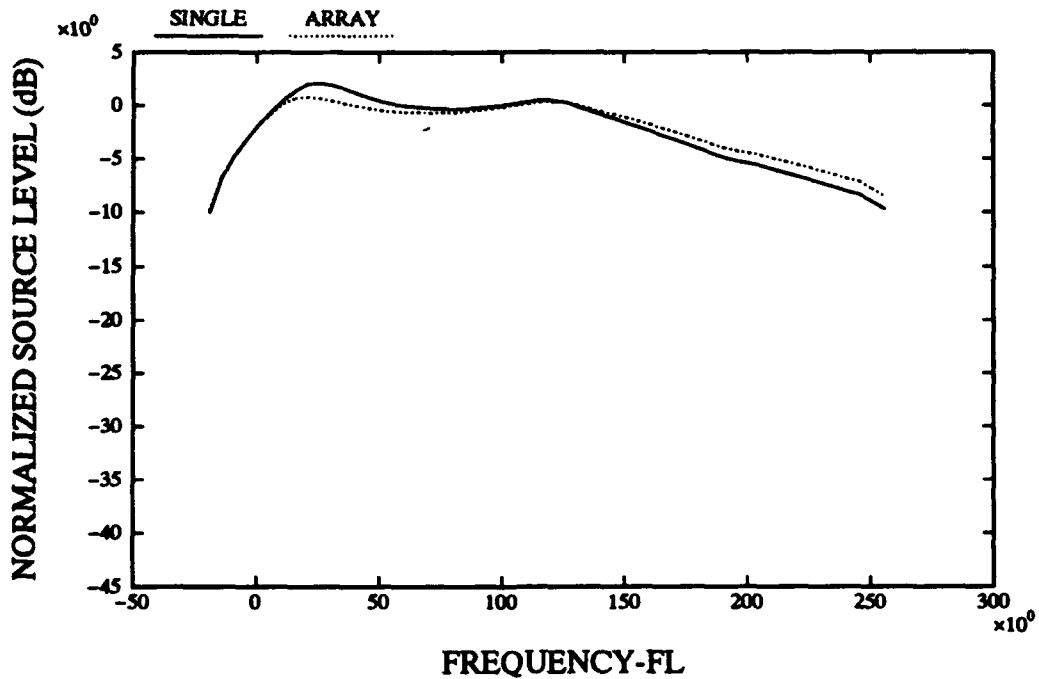


Figure 37. Normalized source level, single element vs array.

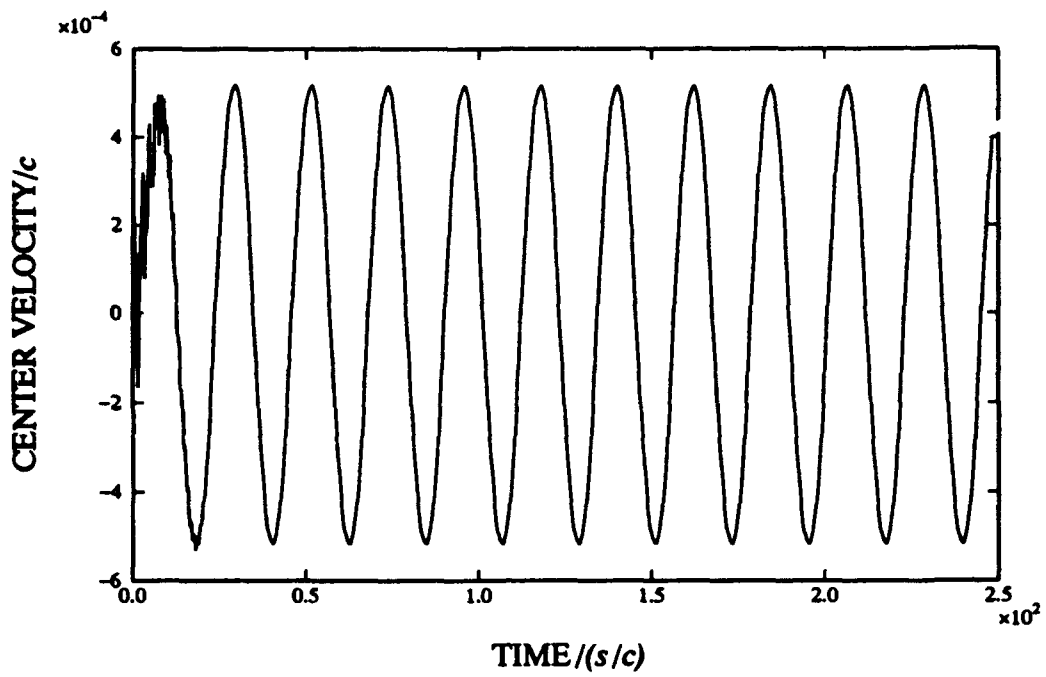


Figure 38. Velocity of middle element of three-element array at freq=FL.

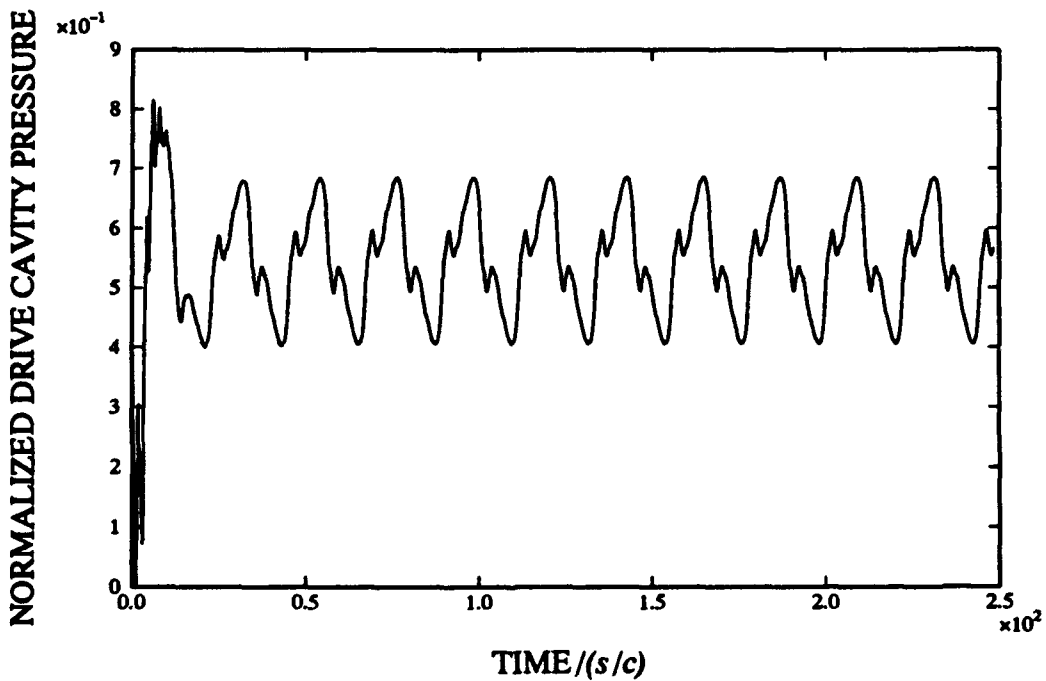


Figure 39. Drive cavity pressure of middle element of three-element array at freq=FL.

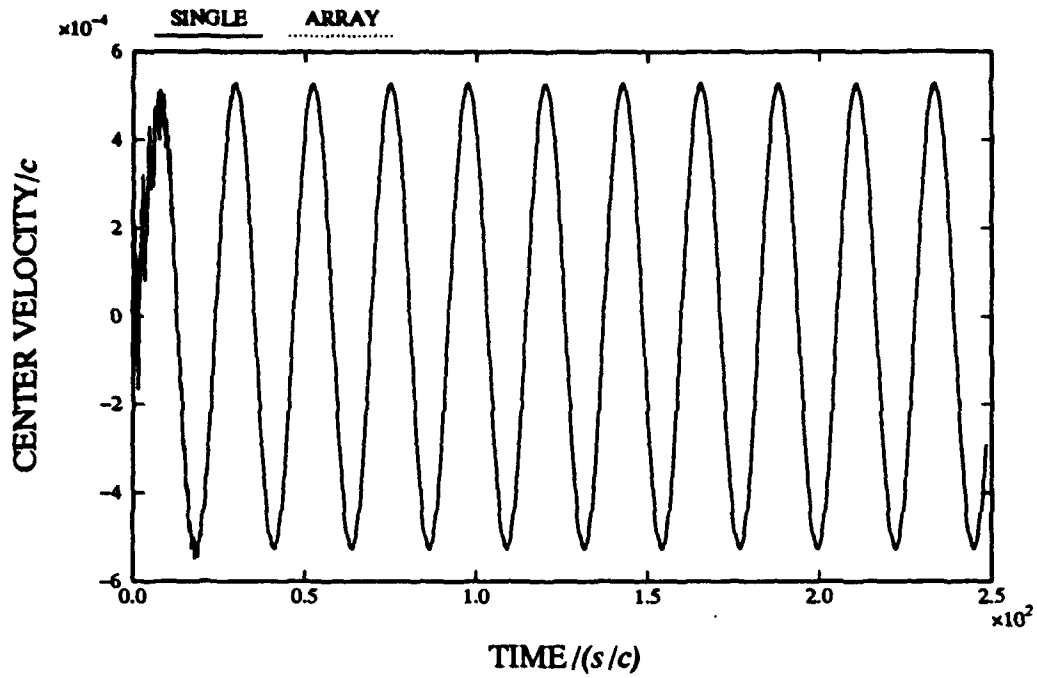


Figure 40. Velocity comparison, middle element of  $1 \times 6$  array vs single element.

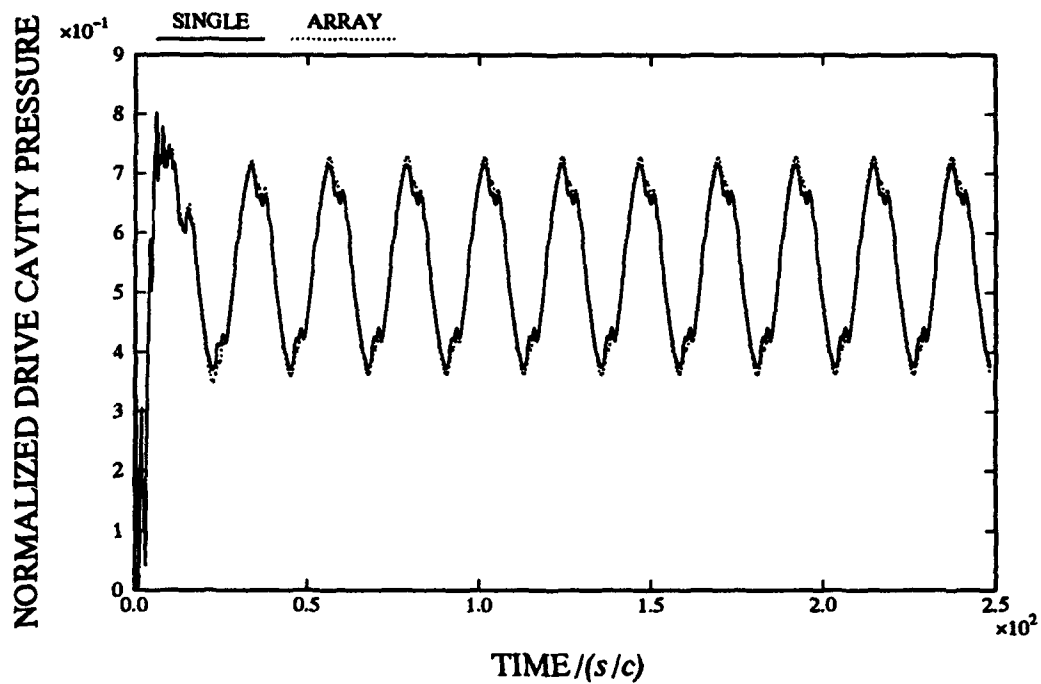


Figure 41. Drive cavity pressure comparison, middle element of  $1 \times 6$  array vs single element.

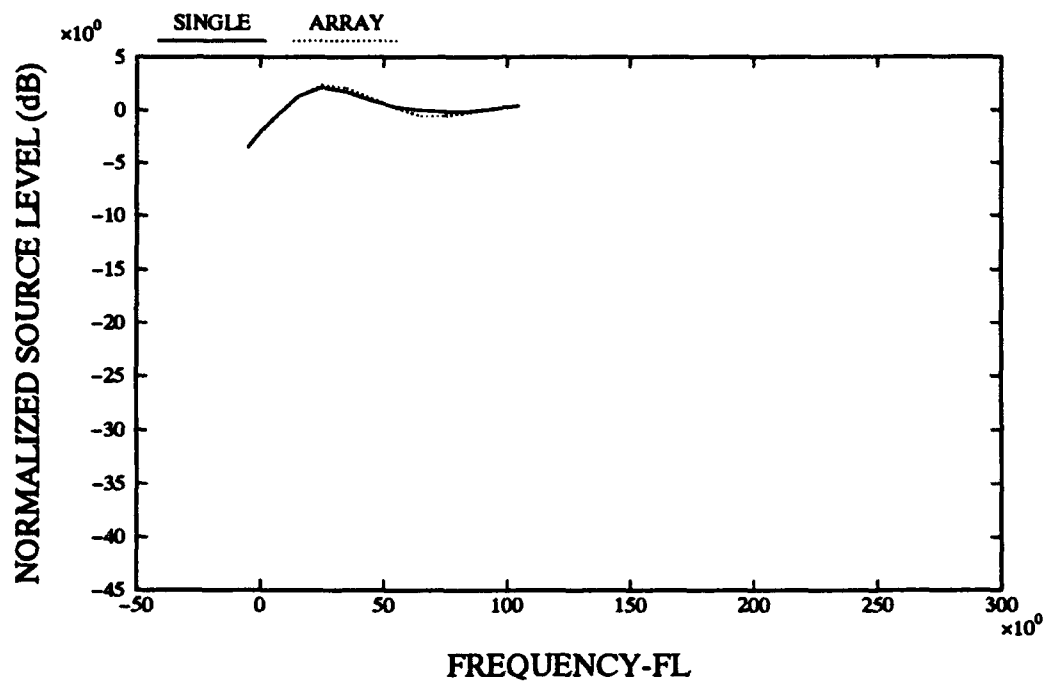


Figure 42. Normalized source level, single element vs six-element array.

## 4 CONCLUSIONS AND RECOMMENDATIONS

A mathematical model has been derived for an array of hydroacoustic transducers and applied to the HLF-6A. The major new feature of this model is the time-domain approach to the array acoustic interaction problem. This approach has been validated for an array of simple linear transducers by comparison with a frequency-domain approach. This linear problem was also used to study the effects of internal damping on the time required to reach steady state. It was found that when the damping was small the time to reach steady state could be very long compared with that of a single element. As the damping was increased, the time to reach steady state decreased dramatically and the steady state level became lower. Results for a single HLF-6A transducer have been compared with corresponding results from HAI's computer model. The agreement is in general very good. Slight differences are attributable to differences in the way acoustic radiation loading is handled. The results of our time-domain model were also compared with experimental results for a close-packed three-element array. The comparison showed the same general trends and levels, but appeared to be slightly shifted in frequency. A proposed, wide-spaced, six-element array was also modeled. At this proposed spacing the interaction effects were minimal. In both the three- and six-element arrays the time to reach steady state was about the same as for a single element since the internal damping of the valve is large.

In the future we would like to investigate an alternative approach in which the interactions are modeled at the drive point impedance level instead of at the radiation impedance level. This would avoid the difficulty of choosing which modes to incorporate in the model. We would also like to further modularize our computer code so that other differential equation solvers could be employed.

## 5 REFERENCES

1. Benthien, G., "A Mathematical Model For A Hydroacoustic Transducer," Naval Ocean Systems Center, San Diego, CA, Technical Report 588, March 1982.
2. Schenck, H., *Improved Integral Formulation for Acoustic Radiation Problems*, J. Acoust. Soc. Am., vol. 44, 1968, pp. 41-58.
3. Benthien, G.W., D. Barach, and D. Gillette, "CHIEF Users Manual," Naval Ocean Systems Center, San Diego, CA, Technical Document 970, September 1988.
4. Golub, G.H. and J.M. Ortega, *Scientific Computing and Differential Equations*, Academic Press, San Diego, CA, 1992, pp. 26-30.
5. Blackburn, J.F., *Fluid Power Control*, Blackburn, J.F., Reethof, G., and Shearer, J.L. eds., Technology Press of M.I.T. and John Wiley & Sons, New York, NY, 1960, p. 300.

# REPORT DOCUMENTATION PAGE

Form Approved  
OMB No. 0704-0188

Public reporting burden for this collection of information is estimated to average 1 hour per response, including the time for reviewing instructions, searching existing data sources, gathering and maintaining the data needed, and completing and reviewing the collection of information. Send comments regarding this burden estimate or any other aspect of this collection of information, including suggestions for reducing this burden, to Washington Headquarters Services, Directorate for Information Operations and Reports, 1215 Jefferson Davis Highway, Suite 1204, Arlington, VA 22202-4302, and to the Office of Management and Budget, Paperwork Reduction Project (0704-0188), Washington, DC 20503

1. AGENCY USE ONLY (Leave blank)	2. REPORT DATE <p style="text-align: center;">May 1994</p>	3. REPORT TYPE AND DATES COVERED <p style="text-align: center;">Final: 1 Jul 1993 to 31 Mar 1994</p>	
4. TITLE AND SUBTITLE <p style="text-align: center;">TIME-DOMAIN MODEL FOR A HYDROACOUSTIC TRANSDUCER ARRAY</p>		5. FUNDING NUMBERS <p style="text-align: center;">PE 0603747N DN309127</p>	
6. AUTHOR(S) <p style="text-align: center;">George W. Benthien and Don Barach</p>		8. PERFORMING ORGANIZATION REPORT NUMBER <p style="text-align: center;">TR 1654</p>	
7. PERFORMING ORGANIZATION NAME(S) AND ADDRESS(ES) Naval Command, Control and Ocean Surveillance Center (NCCOSC) RDT&E Division San Diego, CA 92152-5000		10. SPONSORING/MONITORING AGENCY REPORT NUMBER	
9. SPONSORING/MONITORING AGENCY NAME(S) AND ADDRESS(ES) Space and Naval Warfare Systems Command SPAWAR PMW 182-32 Washington, DC 20363-5200		11. SUPPLEMENTARY NOTES	
12a. DISTRIBUTION/AVAILABILITY STATEMENT <p style="text-align: center;">Approved for public release; distribution is unlimited.</p>		12b. DISTRIBUTION CODE	
13. ABSTRACT (Maximum 200 words)  <p>This report contains a description of a mathematical model for a hydroacoustic transducer array. Previous models have attempted to couple frequency-domain models for the acoustic field with time-domain models for the internal components of the transducer. In this report, we present a complete time-domain model for the coupled transducer/acoustic-field problem that is applicable to both single elements and arrays. This model can also handle nonsinusoidal signals, which is important since linear superposition is not valid for nonlinear devices. The acoustic radiation model involves obtaining certain interaction coefficients in the frequency domain and then transforming these coefficients to the time domain by using Fourier transforms. When these coefficients are combined with a model for the internal components, the result is a coupled set of differential-integral equations that can be solved by an explicit time-stepping procedure. For purposes of validation, the time-domain acoustic-radiation model was applied to a simple linear transducer array for which the solution could also be obtained by the standard frequency-domain approach. The agreement between the two approaches was excellent. The time-domain model was also compared with experimental data for a three-element close-packed array. The agreement was reasonably good in both level and trends.</p>			
14. SUBJECT TERMS  acoustic interactions      transducer nonlinear array            transient time-domain			15. NUMBER OF PAGES <p style="text-align: center;">57</p>
17. SECURITY CLASSIFICATION OF REPORT <p style="text-align: center;">UNCLASSIFIED</p>			16. PRICE CODE
18. SECURITY CLASSIFICATION OF THIS PAGE <p style="text-align: center;">UNCLASSIFIED</p>	19. SECURITY CLASSIFICATION OF ABSTRACT <p style="text-align: center;">UNCLASSIFIED</p>	20. LIMITATION OF ABSTRACT <p style="text-align: center;">SAME AS REPORT</p>	

UNCLASSIFIED

21a. NAME OF RESPONSIBLE INDIVIDUAL George W. Benthien	21b. TELEPHONE (include Area Code) (619) 553-1463	21c. OFFICE SYMBOL Code 711

## INITIAL DISTRIBUTION

Code 0012	Patent Counsel	(1)
Code 0274	Library	(2)
Code 0275	Archive/Stock	(6)
Code 574	T. Mautner	(1)
Code 70	T. F. Ball	(1)
Code 702	H. A. Schenck	(1)
Code 71	J. M. Holzmann	(1)
Code 7106	P. W. Leupold	(1)
Code 711	E. F. Rynne, Jr.	(1)
Code 711	G. W. Benthien	(10)
Code 711	D. Barach	(10)
Code 711	S. Nichols	(1)
Code 711	W. F. Rask	(1)
Code 711	J. DeJaco	(1)
Code 711	D. L. Gillette	(1)
Code 711	J. Culver	(1)
Code 712	C. L. Meland	(1)
Defense Technical Information Center		
Alexandria, VA 22304-6145		(4)
NCCOSC Washington Liaison Office		
Washington, DC 20363-5100		
Center for Naval Analyses		
Alexandria, VA 22302-0268		
Navy Acquisition, Research and Development		
Information Center (NARDIC)		
Arlington, VA 22244-5114		
GIDEP Operations Center		
Corona, CA 91718-8000		
Naval Research Laboratory		
Underwater Sound Reference Detachment		
Orlando, FL 32856-8337		(2)
Naval Undersea Warfare Center		
New London, CT 06320-5594		(2)
Space and Naval Warfare Systems Command		
2451 Crystal Drive		
Arlington, VA 22245-5200		(2)
Naval Postgraduate School		
Monterey, CA 93943-5100		
Alliant Techsystems, Inc.		
Mukilteo, WA 98275-4844		(2)
General Electric Corporate Research and Development		
Schenectady, NY 12301		
Hydroacoustics, Inc.		
Rochester, NY 14692		